Dissipation in a finite-temperature atomic Josephson junction

K. Xhani [1,2] and N. P. Proukakis [1]

[1] *Joint Quantum Centre (JQC) Durham-Newcastle, School of Mathematics, Statistics and Physics, Newcastle University, Newcastle upon Tyne NE1 7RU, United Kingdom*

[2] *CNR-INO, European Laboratory for Non-Linear Spectroscopy (LENS), 50019 Sesto Fiorentino, Italy*

(Received 2 October 2021; revised 16 July 2022; accepted 19 July 2022; published 13 September 2022)

We numerically demonstrate and characterize the emergence of distinct dynamical regimes of a finite-temperature bosonic superfluid in an elongated Josephson junction generated by a thin Gaussian barrier over the entire temperature range where a well-formed condensate can be clearly identified. Although the dissipation arising from the coupling of the superfluid to the dynamical thermal cloud increases with increasing temperature as expected, the importance of this mechanism is found to depend on two physical parameters associated (i) with the initial chemical potential difference, compared to some characteristic value, and (ii) the ratio of the thermal energy to the barrier amplitude. The former determines whether the superfluid Josephson dynamics are dominated by gradually damped plasmalike oscillations (for relatively small initial population imbalances), or whether dissipation at early times is instead dominated by vortex- and sound-induced dissipation (for larger initial imbalances). The latter defines the effect of the thermal cloud on the condensate dynamics, with a reversal of roles, i.e., the condensate being driven by the oscillating thermal cloud, being observed when the thermal particles acquire enough energy to overcome the barrier. Our findings are within current experimental reach in ultracold superfluid junctions.

DOI: 10.1103/PhysRevResearch.4.033205

I. INTRODUCTION

Josephson effects across a junction separating two parts of a quantum liquid [1,2] are ubiquitous in nature, occurring across superconductors [1–3], superfluid helium [4–7], trapped ultracold atomic gases [8–21], and exciton-polariton condensates [22,23]. The most characteristic manifestation of Josephson junctions in ultracold atomic systems relates to the so-called "plasma" oscillations associated with periodically alternating particle transfer across the junction with a population difference and an associated relative phase between the two sides of the junction oscillating about a zero value. Such behavior has been observed in a range of experiments, including ultracold bosonic atoms in diverse geometries [9,10,12,14–16] and fermionic superfluids across the BEC-BCS crossover [17–21], with atomic current across a Josephson junction playing an important role in atomtronics [24–28].

As the underlying features are of a quantum nature, associated with the densities and phases of the superfluids across the two sides of the junction, most theoretical treatments to date have focused on the more fundamental, pure superfluid (zero-temperature) analysis. The dynamics of such atomic systems was first analyzed in Refs. [29,30], which predicted two distinct regimes, with the analysis based on a two-mode model and a corresponding analogy to the nonrigid pendulum with variable length with more detailed theoretical/numerical analysis conducted by various authors [31–35]. Specifically, the work of Refs. [29,30] highlighted the existence of a "self-trapping" regime characterized by population imbalance oscillations about a nonzero value (i.e., one side of the junctions always maintains a higher population than the other), associated with a relative phase increasing in time (rather than an oscillating phase). Such a regime, was first observed in Ref. [10], followed by related experiments in other groups [14,15].

Viewed differently, the Josephson junction separating two parts of a superfluid can also be viewed as a barrier acting against the underlying superflow: as such, superflow dissipation can emerge even strictly at $T = 0$ by the generation of sound waves, and even nonlinear excitations, such as solitons [36,37], vortices [17,18,38–42], and shock waves [37,43], depending on system geometry and dimensionality. Such dynamical excitation features across a Josephson junction, which are well-known as phase slips in the context of superconductors [44,45], superfluids [4,7], and ultracold transport [28,33,36,38,40,41,46,47], have also been observed in recent ultracold experiments with fermionic superfluids [17,18]. Such behavior has been previously analyzed in depth by the present authors [38], thus shedding more light on the microscopic and energetic origins of dissipation in such systems, and directly connecting microscopic findings with experimental observations both for coherent and dissipative transport across an ultracold Josephson junction.

The combination of earlier experimental and theoretical works thus indicated two distinct transitions from the Josephson "plasma" regime with increasing initial population imbalance, namely to either the self-trapped or to the phase-slip-induced dissipative dynamical regimes. The former, "self-trapped," regime is generally expected to emerge in the limit of validity of the two-mode model [29,30,32,48–53], i.e., in the limit of rather high barriers, compared to the system's chemical potential. To better understand the conditions leading to either of these two dynamical transitions, the present authors undertook a detailed systematic analysis of the phase diagram of the dynamical regimes across a Josephson junction as a function of initial population imbalance, barrier properties, and underlying system geometry [39]. Our findings clearly characterized the nature of the transition of the Josephson oscillations with increasing population imbalance as being "dissipative" in the limit of relatively low/narrow barriers, and "self-trapped" in the opposite regime of high/wide barriers, with a complicated intermediate regime featuring irregular population/phase dynamics, thus providing a complete characterization of the emergence of such different dynamical regimes.

While such work thoroughly addressed the $T = 0$ pure superfluid dynamical regimes, few studies to date have studied the effects of thermal, or quantum, excitations [31,36,50,54–62]. This can be crucial, since experiments are typically performed at small, but nonzero, temperatures $T \ll T_c$ (where T_c is the critical temperature for Bose-Einstein condensation): in fact, evidence of thermal dissipation in the self-trapped regime has already been experimentally observed in [14]. It is thus of significant interest to understand the role of the thermal cloud on the junction dynamics. Some work on the decay of the self-trapped regime has been performed in the context of the dissipative and stochastic projected Gross-Pitaevskii equation [54], qualitatively reproducing the findings of Ref. [14].

In the present work, we provide a unified characterization of the fundamental role of thermal dissipation in both the Josephson plasma and the dissipative regimes by means of a self-consistent theory that incorporates a dynamical thermal cloud and its backaction on the condensate. Specifically, we perform a detailed analysis of the long-term dissipative dynamical evolution of the superfluid across a Josephson junction, focusing on the relative population dynamics, their dominant frequencies, and the relation between condensate and thermal cloud dynamics. We identify two distinct dynamical regimes, namely a low-temperature regime in which the small thermal cloud is driven by the condensate, and a high-temperature regime in which the thermal cloud has enough energy to overcome the barrier, and thus begins to drive the condensate. The dominant frequencies identified are the Josephson plasma frequency (slightly lower than the trap frequency), a frequency we interpret as its corresponding second-order contributions, and the dipolar frequency of the thermal cloud (which is close to the underlying harmonic trap frequency). All such frequencies are found to be relevant in both the Josephson plasma and the dissipative regimes, with their relative importance dependent both on the dynamical regime and on temperature, as we shall discuss.

This paper is structured as follows: Section II introduces the key concepts required for our analysis, namely the physical system and geometry (Sec. II A), and a brief summary of the underlying dynamical regimes in the limit of a pure superfluid (Sec. II B) and of the documented importance of second-order tunneling contributions to date (Sec. II C), with the dynamical finite-temperature model used summarized in Sec. II D. Section III summarizes the parameter regime of this study and identifies the physical observables that are used to analyze the emerging dynamics across the entire temperature domain (Sec. III A), analyzing the system dynamics, dominant frequency components, and damping rates in both the Josephson (Sec. III B) and dissipative regimes (Sec. III C) at a fixed condensate number, further highlighting the role of the thermal cloud on the damping of sound waves. Our findings on the finite-temperature dynamical regimes are revisited in Sec. IV in the context of fixed total particle number, with our observations further discussed and concluded in Secs. V and VI, respectively.

II. PHYSICAL SYSTEM AND $T > 0$ KINETIC MODEL

A. Gaussian junction in an elongated anisotropic harmonic trap

The physical system considered in this study is an anisotropic highly elongated harmonic trap, with a double-well potential of the form

$$V_{\rm ext}(x,y,z) = \frac{1}{2}M\left(\omega_x{}^2x^2 + \omega_y{}^2y^2 + \omega_z{}^2z^2\right) + V_0\, e^{-2x^2/w^2}. \quad (1)$$

This geometry is motivated by the LENS fermionic superfluid experiments, which observed the dissipative regime, with our analysis restricted to the BEC limit of lithium molecules [17,18]. As such, and consistent with our earlier works [38,39], our study uses trapping frequencies $\omega_x = 2\pi \times 15$ Hz, $\omega_y = 2\pi \times 148$ Hz, and $\omega_z = 2\pi \times 187.5$ Hz across the x, y, and z directions, respectively. To avoid a potential change in the system dynamical regime caused by a changing condensate particle number with varying temperature, our primary finite-temperature study is conducted at a fixed condensate particle number, $N^{\rm BEC} = (5.04 \pm 0.02) \times 10^4$. The small error bar is given by the maximum difference between the condensate number at different T, and it has no noticeable effect on our characterization of the Josephson junction dynamics. We also keep fixed the barrier height $V_0 = 104\hbar\omega_x$ and width $w = 2$ μm. In the pure superfluid limit ($T = 0$), this amounts to $V_0 = 0.97\mu$ and $w = 3.8\xi$, where $\xi = \hbar/\sqrt{2\mu M} = 0.52$ μm denotes the condensate healing length. For these parameters, the system cannot support the emergence of macroscopic quantum self-trapping, and only the Josephson plasma and the dissipative regimes are found. Moreover, smaller values of V_0/μ would imply being more in a hydrodynamical than a tunneling regime.

A schematic of the initial system density for such parameters is shown in Fig. 1 for $T = 0$ [pure condensate, Fig. 1(a)] and $T = 0.58T_c$ [Fig. 1(b)]: in the latter case, the top panel (i) shows the condensate, with the corresponding thermal cloud contribution shown—within the context of the Hartree-Fock approximation—in panel (ii), clearly revealing the thermal cloud surrounding the condensate and partly infilling the barrier region where the condensate contribution decreases. More

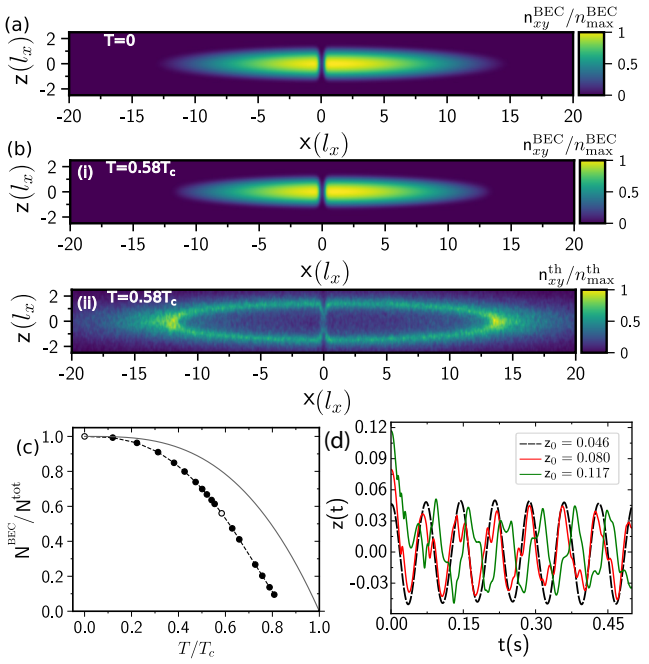

FIG. 1. (a) Equilibrium 2D integrated condensate density in the xz-plane at $T = 0$ (which coincides with the total density). (b) The corresponding equilibrium integrated (i) condensate and (ii) thermal cloud density profiles in the xz-plane at $T = 88$ nK $= 0.58T_c$ for the same fixed condensate number $N^{\rm BEC} \simeq 5.04 \times 10^4$ and $V_0/\mu(T = 0) = 0.97$. All densities are scaled to their corresponding maximum values, as indicated by the color bars. (c) Condensate fraction as a function of the temperature T scaled to the noninteracting critical value $T_c = T_c[N(T)]$ for the corresponding total particle number $N(T)$ in each case (circles), showing the entire regime of temperatures probed in our present analysis: the cases $T = 0$ and $0.58T_c$, whose corresponding densities were shown, respectively, in (a) and (b), are indicated as hollow circles, and the dashed line is a guide to the eye. The thin solid gray line shows the corresponding ideal-gas analytical prediction. (d) Time evolution of the population imbalance at $T = 0$ for different values of z_0: (i) for an initial imbalance z_0 just below $z_{\rm cr}$ the system exhibits undamped Josephson plasma oscillations (black dashed line); (ii) at $z = z_{\rm cr}$, corresponding to the critical imbalance for the onset of the dissipative regime, with a single vortex ring generated (red line); (iii) $z_0 > z_{\rm cr}$, showing kinks characteristic of the sequential generation of multiple vortex rings (green line).

details of our theoretical model are discussed in Sec. II D and Appendix A. The dependence of the condensate fraction on (scaled) temperature over which such dynamical behavior is characterized is shown in Fig. 1(c). As our analysis is performed with a fixed *condensate* particle number at different temperatures, this implies that the thermal, and thus total, particle number $N = N(T)$ increases with increasing temperature; for this reason, each point on this graph has been scaled by its own corresponding noninteracting harmonically trapped three-dimensional (3D) critical temperature $T_c = T_c[N(T)] \simeq 0.94 \times (\hbar\bar{\omega}/k_B)[N(T)]^{1/3}$ [where $\bar{\omega} = (\omega_x\omega_y\omega_z)^{1/3}$] [63]. For comparison, we also plot the noninteracting prediction for the condensate fraction, which confirms the expected shift of the critical region due to finite-size and mean-field corrections [63]. As is evident from Fig. 1(c), our analysis is performed over a very broad temperature range, in which there is at least a 10% condensate fraction, thus avoiding limitations of our approach as the system approaches the critical region.

To compute the initial equilibrium imbalanced state, we apply a linear barrier shift $-\epsilon x$ to the double-well potential. This is subsequently instantaneously removed, at $t = 0$, in order to initiate the dynamics that we probe. The shift ϵ is kept the same for all temperatures considered throughout our analysis, thus fixing the initial condensate imbalance (a subtle shift at rather high T will be commented upon later, in Sec. III and Appendix E).

B. Josephson plasma oscillations versus dissipative dynamics at $T = 0$

As is well known, a pure ($T = 0$) superfluid system with an initial population imbalance across the junction can exhibit undamped oscillatory particle transfer across the junction (for a given barrier height/width configuration) with plasma frequency ν_J [shown in Fig. 1(d) by the black dashed line]. This is typically characterized by the fractional population imbalance

$$z(t) = \frac{N_R(t) - N_L(t)}{N_R(t) + N_L(t)}, \tag{2}$$

where $N_{R/L}$ is the number of condensate particles on the right/left sides of the barrier (centered at $x = 0$); the time derivative of this quantity gives the superfluid current across the junction, via the expression $I = -(N/2)dz(t)/dt$, with $N = N_R + N_L$ being the total particle number.

Increasing the initial population imbalance for our parameters actually leads to flow speeds exceeding the local critical velocity, thus inducing the dissipation of superflow kinetic energy through the generation of vortex rings and associated sound waves, an effect already interpreted in our previous work [38,39], and observed experimentally [17,18]. This is the so-called dissipative regime, characterized by a rapid initial decay of the population imbalance, followed by oscillations around a zero value with one or more frequencies. The emergence of such behavior can be clearly seen in the evolution of the population imbalance corresponding to the red and green curves in Fig. 1(d).

As a first step, we explicitly calculate for our parameters the critical population imbalance marking the transition from Josephson plasma to the phase-slip-induced dissipative regime (shown in Appendix C). At $T = 0$ and for each barrier height value, we define $z_{\rm cr}^{\rm BEC}$ as the first explored value of initial imbalance at which the imbalance amplitude exhibits (within $t \sim 0.1$ s) exactly one kink (indication of the backflow associated with the generation of a vortex ring [38,39]), while simultaneously the relative phase undergoes one phase-slippage mechanism; such behavior is shown by the red profile in Fig. 1(d). Further increase in the population imbalance leads to sequential generation of multiple vortex rings across the junction during the early phase of unidirectional flow across the junction, as can be seen by the green line showing the case of an initial population imbalance well above the critical value for the chosen parameters. We use the same criterion to identify the critical condensate population imbalance in the case of finite T. Indeed, in Appendix C we show that fixing the condensate particle number implies the transition is

(within numerical error) unaffected by the presence of thermal particles for all barrier heights probed.

Furthermore, we note that the condensate dynamical regime across the Josephson junction depends on the value $V_0/\mu(T=0)$, where $\mu(T=0)$ is the zero-temperature chemical potential obtained by the Gross-Pitaevskii equation in the limit of all particles being in the superfluid. Given that $\mu(T=0)$ is held fixed throughout our simulations, all our analysis is thus done at fixed $V_0 = 0.97\mu(T=0)$.

For completeness, we note here that the third dynamical regime, namely self-trapping, is not relevant to this work, as—for our parameter set—it manifests itself at a much higher value of $V_0/\mu(T=0) \simeq 1.7$.

In the subsequent analysis of Sec. III, we will consider those two regimes separately (Secs. III C and III D, respectively) to focus on the role of the thermal cloud on particle dynamics.

C. Second-order Josephson junction contributions

Given that our study identifies more than one relevant superfluid oscillation frequency, both at $T=0$ and in the $T>0$ regimes, it is appropriate here to briefly summarize prior relevant work identifying such multiple frequencies and the role of their arising couplings [19,20,38,55,61,64–67].

At first order in the tunneling Hamiltonian, only the condensate-to-condensate tunneling term contributes to the superfluid current, and the current-phase relation is sinusoidal, $I = I_c \sin(\Delta\phi)$. This is valid as long as the barrier height is much larger than μ. However, if instead $V_0 \sim \mu$, second-order terms must be considered that originate from the tunneling between condensate and noncondensate states. At $T=0$ and for a BEC, the latter consists of phonon modes [31,55].

In the presence of a finite chemical potential difference between the two wells, this second-order term could lead to the presence of an additional nondissipative [of the form "$\sin(2\Delta\phi)$"] and/or dissipative term [of the form "$\cos(2\Delta\phi)$"] in the current-phase relation, with the latter being finite even at $T=0$. The presence and importance of the coherent (nondissipative) term oscillating at double the ν_J frequency has been studied in several papers both with bosonic and fermionic systems [19,20,38,55,61,64]. Moreover, for our geometry, Ref. [38] shows that the profile of the maximum superfluid current flowing through the junction versus the barrier height V_0/μ could be described by the presence of both the first-order ["$\sin(\Delta\phi)$"] and the nondissipative second-order ["$\sin(2\Delta\phi)$"] term in the current-phase relation, with the second having a negative sign. In fact, a recent study with a point-contact junction [68] shows the presence even of a dissipative current term in that geometry, as predicted by [55].

In the following sections, we will show that our analysis, based on the long-time evolution of the superfluid dynamics, suggests that both dissipative and nondissipative second-order terms in the superfluid current (i.e., population imbalance) could become important, and their presence depends on the dynamical regime. For completeness, we also note here that the multimode regime is also found in the highly excited self-trapping regime for an initial imbalance much larger than a critical value [39,65,66].

D. Self-consistent finite-temperature kinetic model

We model the system as the sum of a condensate and a thermal part, in the context of the collisionless Zaremba-Nikuni-Griffin (ZNG) formalism [69–72]. This technique, which has already been successfully applied to diverse nonequilibrium settings, including condensate growth [73], collective modes [74,75], soliton [76], and vortex [77–79] dynamics, is described in more detail in Appendix A. The condensate wave function ψ evolves according to the generalized Gross-Pitaevskii equation

$$i\hbar\frac{\partial\psi}{\partial t} = \left[-\frac{\hbar^2\nabla^2}{2M} + V_{\rm ext} + g(|\psi|^2 + 2n^{\rm th})\right]\psi, \qquad (3)$$

which accounts for the thermal cloud mean-field potential, $2gn^{\rm th}$ [69]. Here M is the particle mass (here the ^{6}Li molecule), $V_{\rm ext}$ is the double-well potential defined above, $g = 4\pi\hbar^2 a/M$ is the interaction strength with a the corresponding s-wave scattering length, and $n^{\rm th}$ is the thermal cloud density. The condensate density is obtained from $n^{\rm BEC} = |\psi|^2$. The thermal cloud dynamics are described through the phase-space distribution f [where $n^{\rm th} = 1/(2\pi\hbar)^3 \int d\mathbf{p}\, f(\mathbf{p},\mathbf{r},t)$], which satisfies the collisionless Boltzmann equation

$$\frac{\partial f}{\partial t} + \frac{\mathbf{p}}{M}\cdot\nabla_{\mathbf{r}} f - \nabla_{\mathbf{r}} V_{\rm eff}^{\rm th}\cdot\nabla_{\mathbf{p}} f = 0, \qquad (4)$$

where $V_{\rm eff}^{\rm th} = V_{\rm ext} + 2g(n^{\rm BEC} + n^{\rm th})$ is the generalized mean-field potential felt by the thermal particles, whose profile is shown in Appendix B.

Due to the repulsive interaction between condensate and thermal particles, the thermal density $n^{\rm th}$ is maximum where the condensate density $n^{\rm BEC}$ is minimum. This is evident in Fig. 1(b), where the thermal cloud (ii) is concentrated at the edges of the condensate density (i) and close to the barrier where $n^{\rm BEC}$ is minimum.

Our numerical study for the superfluid, based on the techniques discussed in Refs. [69,70], is conducted in a grid of $[-24,24]l_x, [-4,4]l_x, [-4,4]l_x$ along the x, y, and z directions, respectively, where $l_x = \sqrt{\hbar/M\omega_x}$, based on $1024\times 64\times 64$ grid points for the condensate. For the more spatially extended thermal cloud, we use a corresponding double grid of size $[-48,48]l_x$, with 2048 grid points along the x axis, further extended to $[-100,100]l_x$, and 2348 grid points for the highest probed temperatures $T\sim 0.8T_c$. The broad temperature range studied here corresponds to a condensate fraction $N^{\rm BEC}/N^{\rm tot} \sim [0.1:1]$ [see Fig. 1(c)].

In this work, we focus on the dynamical evolution of the condensate and total particle number fractional population imbalance across the Josephson and dissipative regimes, and we analyze their dominant contributions and corresponding frequencies of oscillations, which display a range of interesting features.

III. DYNAMICAL REGIMES AT FIXED CONDENSATE NUMBER

A. Physical variables

In this section, we show our results for a fixed condensate particle number. Our parameter choice of barrier height and width here corresponds to a regime in which the generated

vortex ring shrinks rapidly at the barrier location, making it hard to directly visualize the vortex ring. Nonetheless, to confirm the existence of vortex rings at lower values of V_0/μ, for which we have previously found them to be long-lived [39], we have done some analysis at $V_0/\mu \sim 0.6$, which clearly shows the generated vortex ring in the condensate as a region of locally reduced condensate density being infilled by the thermal cloud, consistent with [77–79]—see Appendix D for more details.

To also fix the initial condensate population imbalance when varying temperature, we use a fixed value of ϵ in the linear barrier shift contribution $-\epsilon x$ for each regime (Josephson, dissipative) studied.

We define the condensate $z^{\rm BEC}(t)$, the thermal cloud $z^{\rm th}(t)$, and the total $z^{\rm tot}(t)$ fractional population imbalances, respectively, as

$$z^{\rm BEC}(t) = \frac{N_R^{\rm BEC}(t) - N_L^{\rm BEC}(t)}{N_R^{\rm BEC}(t) + N_L^{\rm BEC}(t)}, \tag{5}$$

$$z^{\rm th}(t) = \frac{N_R^{\rm th}(t) - N_L^{\rm th}(t)}{N_R^{\rm th}(t) + N_L^{\rm th}(t)}, \tag{6}$$

$$z^{\rm tot}(t) = \frac{N_R(t) - N_L(t)}{N_R + N_L} = \frac{N_R(t) - N_L(t)}{N^{\rm tot}}, \tag{7}$$

where $N_{R/L}^{\rm BEC}$ and $N_{R/L}^{\rm th}$ are the number of the condensate and thermal particles on the right/left sides of the barrier (centered at $x = 0$), while $N_{R/L}$ is the sum of the number of thermal particles and condensate particles on the right/left sides of the junction; we also note that, by construction, the total particle number is conserved in our collisionless model.

Having fixed the ratio of V_0/μ, the $T = 0$ limit has a definitive value for the critical population imbalance marking the transition from plasma to dissipative regime; for our current parameters, this occurs at $z_{\rm cr}^{\rm BEC} = 0.08$. The system dynamics in the pure superfluid limit is thus determined by the sign (and magnitude) of $(z_0^{\rm BEC} - z_{\rm cr}^{\rm BEC})$ [38,39]. To clearly analyze the role of temperature on the system dynamics, we choose to avoid potential transient issues very close to the dynamical transition point, and thus conduct our analysis for two fixed values of z_0 chosen as $z_0^{\rm BEC} = 0.046 < z_{\rm cr}^{\rm BEC}$ (Josephson plasma regime) and $z_0^{\rm BEC} = 0.106 > z_{\rm cr}^{\rm BEC}$ (vortex-induced dissipative regime), for which only a few vortex rings are generated.

The presence of a thermal cloud introduces an additional relevant physical parameter for the system dynamics. Specifically, the ratio V_0/k_BT distinguishes between two dynamical regimes for the thermal cloud. For relatively low temperatures $V_0/k_BT \gtrsim 1$, the thermal cloud particles—which would normally be constrained to either side of the barrier having insufficient energy to travel above it (exhibiting incoherent tunneling)—can only propagate through their interaction with the condensed particles. However, in the opposite high-temperature regime $V_0/k_BT \lesssim 1$, the thermal particles have sufficient energy to overcome the barrier, and are thus allowed to execute oscillations in the underlying trap, hindered, but not precluded, by the Gaussian barrier forming the Josephson junction for the superfluid. As such, one would expect—and we indeed find—different dynamical behavior to be dominating the low- and high-temperature regimes, observing a gradual change in the system dynamical behavior around the regime $T \sim V_0/k_B$. In this work, we probe the temperature range $k_BT/V_0 \in [0, 3.1]$, corresponding to $T \in [0, 220]$ nK.

We note that the chosen value V_0 of the barrier height used in our analysis corresponds for the simulated condensate particle number to an effective temperature $V_0/k_B \sim 70$ nK. Noting the changing *total* particle number and T_c with temperature, our analysis is thus conducted in the range $T/T_c \in [0, 0.8]$, with the characteristic thermal energy separating the two thermal cloud dynamical regimes emerging (for the particular geometry and condensate particle number) at $V_0/k_B \sim 0.5T_c$.

Having introduced the physical variables, we now proceed to analyze the role of the thermal cloud on the dynamics in each regime, paying particular attention to the dependence of the plasma frequency on temperature, and the relative importance of this frequency on the system dynamics.

B. $T > 0$ Josephson plasma regime

In general, the Josephson frequency of the condensate population imbalance plasma oscillations is expected to be set by the frequency of the lowest relevant excited state of the system in the combined potential of the underlying trap and barrier, approaching the corresponding oscillatory mode in the trap in the limit of vanishingly small barrier height V_0/μ [80,81]. In a harmonically confined condensate, as considered in this work, it is thus expected to be a fraction of the trapping potential [31]. Correspondingly, in a box potential, the Josephson frequency is a fraction of the sound frequency [37,61], and approaches it for barrier heights approaching zero. In the deep tunneling regime, the oscillation frequency ω_J depends on the characteristic Josephson junction energies, such as the tunneling energy E_J and the on-site interaction energy E_c, with $\omega_J = (1/\hbar)\sqrt{E_cE_J}$ in the two-mode model approximation [29–31,49]. In our present configuration, for which the two-mode model does not in fact predict well the Josephson frequency [38], we extract the relevant frequencies numerically from sinusoidal fits of the time evolution of the condensate imbalance.

We start by analyzing the dependence of the system dynamics on temperature in the Josephson regime, upon fixing the initial *condensate* population imbalance $z_0^{\rm BEC} = 0.046 < z_{\rm cr}^{\rm BEC}$ (with $z_0^{\rm BEC}/z_{\rm cr}^{\rm BEC} \sim 0.6$).

The evolution of the fractional relative population imbalance is shown in Fig. 2 for (a) a low, (b) an intermediate, and (c) a relatively high temperature. At low temperatures the small thermal fraction (red) is moved by the condensate motion, with no significant distinction between the condensate (solid black) and total (solid green) fractional population imbalances, both of which are slightly damped through the mutual friction of the condensate in its motion through the thermal cloud: such damping is evident in Fig. 2(a), which also shows—for comparison—the previously considered $T = 0$ undamped plasma oscillations [dashed black line already shown in Fig. 1(d)].

However, as the temperature increases to values $k_BT > V_0$ [Figs. 2(b) and 2(c)], the increasing thermal component is free

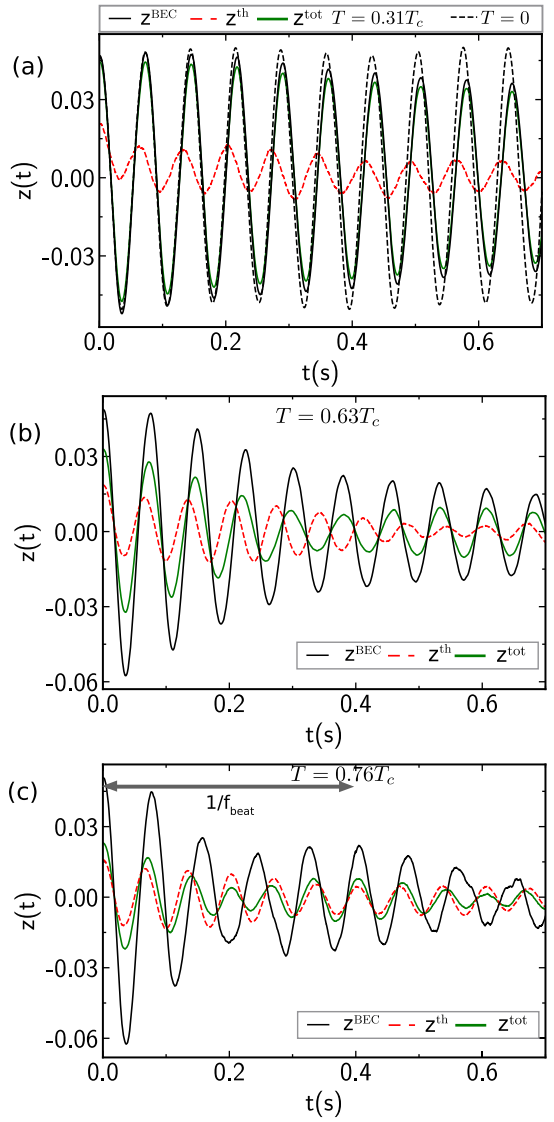

FIG. 2. Population imbalance oscillations exhibiting damping (and, in some cases, beating) for the condensate (black), thermal (red), and total (green) population imbalances in the Josephson regime ($z_0 < z_{cr} = 0.08$) at different temperatures: (a) $T = 40$ nK $= 0.31T_c$, (b) $T = 100$ nK $= 0.63T_c$, and (c) $T = 160$ nK $= 0.76T_c$, where T_c corresponds to the noninteracting critical temperature for the case of a fixed condensate number $N^{BEC} = 5.04 \times 10^4$ (such that T_c varies with T). These data correspond to a Gaussian barrier with $V_0 = 104\hbar\omega_x = 0.97\mu(T = 0)$ and $w = 3.8\xi$. For comparison, the dashed black line in (a) depicts the corresponding undamped single-frequency Josephson plasma oscillations in the pure superfluid ($T = 0$) limit, which corresponds to the black dashed line in Fig. 1, i.e., $z_0 = 0.046$.

to execute its own oscillations over the barrier, at a distinct frequency from that of condensate oscillations. As a result, the condensate oscillations are significantly damped, and the total population difference oscillation features becomes more similar to those of the thermal imbalance, with the combination of the two distinct frequencies leading to the emergence of beating. The higher the temperature, the shorter the beating time is, i.e., its corresponding frequency f_{beat} is larger, thus favoring its observation even within experimental times. The reason for that will be clearer in the following sections.

At low T the thermal cloud mean kinetic energy k_BT is not high enough for the thermal cloud to flow hydrodynamically through the barrier. Thus thermal particles can only perform incoherent tunneling through the barrier [31,54]. For relatively low T such that the thermal cloud mean kinetic energy k_BT is smaller than or comparable to $(V_0 - \tilde{\mu})$, the crossing rate of a thermal particle across the barrier is given by the Arrhenius-Kramers formula:

$$P_{th} \simeq \frac{\omega_x}{2\pi} \exp\left(-\frac{(V_0 - \tilde{\mu})}{k_BT}\right), \tag{8}$$

where $\tilde{\mu} = \mu(N/2)$ [31].

For the chosen barrier height, which is close to $\tilde{\mu}$, Eq. (8) is valid for $T \lesssim 15.4$ nK. For our lowest nonzero temperature data point, $T = 15$ nK $\simeq 0.1T_c$, Eq. (8) estimates a crossing rate $P_{th} \sim 5.4$ Hz, which corresponds to a time $\tau_{th} \sim 0.19$ s. This means that each $\sim$0.19 s, thermal particles may cross the barrier via tunneling.

Closer inspection of the superfluid oscillations reveals contributions from more than one frequency, even at low temperatures. This might have been expected as in our parameter regime ($V_0/\mu \simeq 1$ and $w/\xi \simeq 4$), which is not in the deep tunneling regime, the superfluid current (thus the condensate imbalance) is expected to oscillate with two frequencies, namely a dominant Josephson plasma frequency and an additional second frequency arising from the second-order term in the tunneling amplitude [55].

Moreover, at finite T, the presence of the thermal cloud introduces a normal component I_n to the Josephson current (an Ohmic-like contribution) [31,55] $I_n = -G_{th}\Delta\mu$, where G_{th} is the junction conductance. In the limit of low T, the latter can be estimated from the Arrhenius-Kramers formula as $G_{th} = \hbar P_{th} N^{th}/(k_BTN^{tot})$ [31,54], with $\Delta\mu$ the chemical potential difference between the two wells being proportional to the condensate imbalance [i.e., $\Delta\mu(t) = E_c z^{BEC}(t) N^{BEC}/2$]. Based on these two considerations, and knowing that the condensate current is related to the condensate imbalance through $I = -(N^{BEC}/2)\, dz^{BEC}/dt$, we then choose as our fitting function for the condensate imbalance a function of the form

$$F(t) = a_J \cos(2\pi\nu_J t + \phi_J) \exp(-\gamma_J t) + a_i \cos(2\pi\nu_i t + \phi_i) \exp(-\gamma_i t), \tag{9}$$

which, in addition to distinct amplitudes ($a_\cdot$), frequencies ($\nu_\cdot$), and damping rates ($\gamma_\cdot$) for the two components (where the dot subscript denotes either J or i), also allows for unconstrained phases $\phi_\cdot$ of each contribution.

First, we focus on the condensate $z^{BEC}(t)$ oscillations, and their dependence on temperature. Examination of both Fourier transforms and the above functional fits reveal, as expected, periodic oscillations at a dominant frequency—which we interpret as the Josephson plasma frequency, labeled by the subscript J, along with a clearly identified secondary frequency over the entire temperature range probed.

Interestingly, the secondary oscillations (labeled here by $i = 1, 2$) correspond to distinct frequencies at low temperatures $k_BT/V_0 \lesssim 1$ (henceforth labeled as ν_1) and high temperatures $k_BT/V_0 \gtrsim 1$ (henceforth labeled as ν_2). To

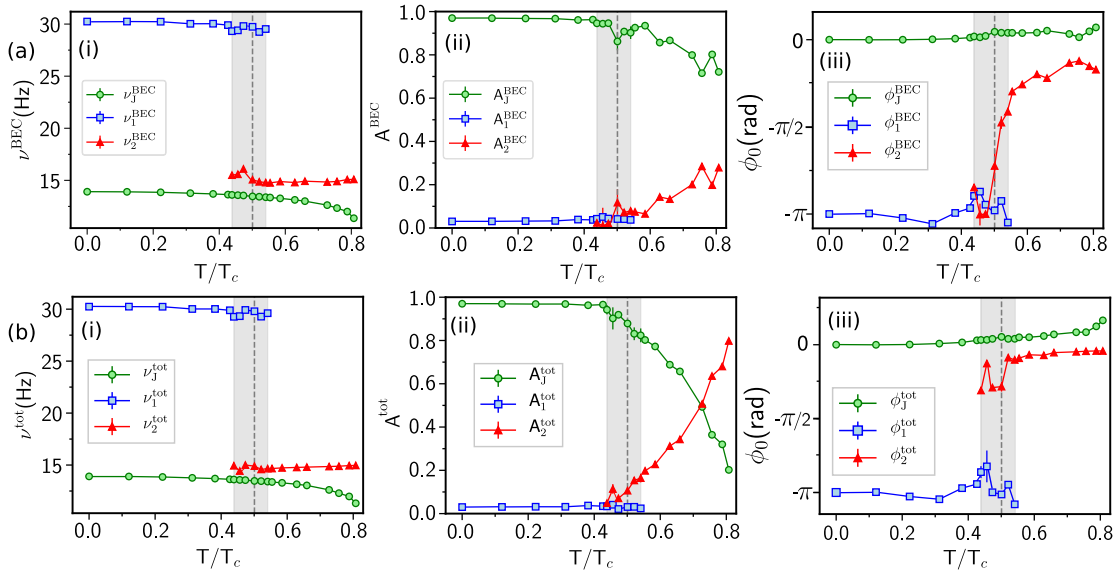

FIG. 3. Temperature dependence of oscillatory dynamics of (a) the condensate, and (b) the total population imbalance across a Josephson junction for a system of fixed condensate particle number, barrier amplitude $V_0/\mu \sim 0.97$, and initial condensate imbalance $z_0 < z_{\rm cr}$ (such that the pure superfluid dynamics are in the Josephson dynamical regime). Shown in each case are (i) the dominant oscillation frequencies, (ii) their relative amplitudes [extracted from Eqs. (9) and (10)], and (iii) their corresponding initial phases [extracted through the fits of Eq. (9)] as a function of scaled temperature. The vertical dashed lines indicate the temperature corresponding to the barrier height, i.e., $T = V_0/k_B = 70$ nK, which corresponds, for the chosen parameters, to $T/T_c \sim 0.5$, with the gray band indicating the region around this characteristic temperature in which there is a transition in the relative importance of different frequency contributions. Population imbalances are fitted in the time interval [0.05 : 0.72] s either by two-frequency fits when two components are clearly predominant (outside the gray band), or by a combination of two- and three-frequency fits in the intermediate region (within the gray band): in the latter case, depicted values and error bars are extracted by averaging over values obtained by the independent two- and three-frequency fits.

capture the transition from ν_1 to ν_2 with increasing temperature, and to avoid introducing any bias to our results, the analysis in a narrow region around $k_BT \sim V_0$ is extended to three-frequency fits (ν_J, ν_1, and ν_2) to provide some continuity to our analysis.

Beyond characterizing the oscillation frequencies and damping rates, we also investigate the relative contributions, $A_.$, of each component defined for the two-component fits as

$$A_J = \frac{a_J}{a_J + a_i} \quad \text{and} \quad A_i = \frac{a_i}{a_J + a_i} \tag{10}$$

(with a_i in the denominator replaced by $\sum_{i=1,2} a_i$ for the case of three-frequency fits). Finally, we investigate the phases $\phi_.$ of the different contributions.

Such information is plotted in Fig. 3 for both (a) the condensate fractional population imbalance $z^{\rm BEC}(t)$ (top plots), and (b) the corresponding total fractional imbalance $z^{\rm tot}(t)$ (bottom panels). In each case, we show the dominant frequencies [left column, (i)], their relative contributions [middle, (ii)], and their individual phases [right, (iii)].

Let us now analyze our findings, focusing initially on the $z^{\rm BEC}(t)$ oscillation frequencies [Fig. 3(a)]: At low $k_BT \ll V_0$, the dominant Josephson dynamics (labeled by green circles) occurs at the frequency $\nu_J \approx 14$ Hz [panel (i)], with a relative weighting exceeding 97% [panel (ii)], and occurring—as expected—without any initial phase delay, i.e., $\phi_J^{\rm BEC} = 0$ [panel (iii)]. As temperature increases towards V_0 (corresponding here to a condensate fraction reduction of ∼30%), the Josephson frequency exhibits a small monotonic decrease on the few % level. The low-temperature frequency $\nu_1 \approx 30$ Hz (blue squares) detectable thus far, with a relative amplitude of a few % and a phase offset of $\sim\pi$, is gradually supplemented by an additional frequency $\nu_2 \approx 15$ Hz, which becomes dominant as temperatures increase beyond $k_BT/V_0 \sim 1$ (indicated by the vertical dashed gray line). At the highest temperature probed here ($k_BT/V_0 \sim 3.1$, $T/T_c = 0.81$), with $N^{\rm BEC}/N^{\rm tot} = 0.1$, the Josephson plasma frequency contribution to the condensate fractional imbalance decreases to about 70%, with the relative phase difference $|\phi_J^{\rm BEC} - \phi_2^{\rm BEC}| \lesssim \pi/4$. We note that the presence of the $\nu_1 \approx 2\nu_J$ frequency component in $z^{\rm BEC}(t)$ even at $T = 0$ with an initial phase $-\pi$ with respect to the ν_J component is consistent with the presence of a second-order (nondissipative) term with an opposing (negative) sign in the current-phase relation. The contribution of such a double Josephson plasma frequency oscillation term [38,55] was previously found to be only a few percent for $V_0 \simeq \mu$ [64], consistent with our current picture.

The above analysis was based entirely on the *condensate* motion, and the backaction that the thermal cloud has on it. Although we have also separately analyzed the thermal cloud population imbalance dynamics, a more complete picture of the coupled system dynamics can be obtained by looking at the imbalance of the total population, $z^{\rm tot}(t)$, with results shown in Fig. 3(b). Again, the same three frequencies are found (ν_J, ν_1, and ν_2) appearing in the same temperature ranges, but there is a critical difference: in our simulations, based on keeping the condensate particle number fixed, the increase in temperature leads to an increase in the number

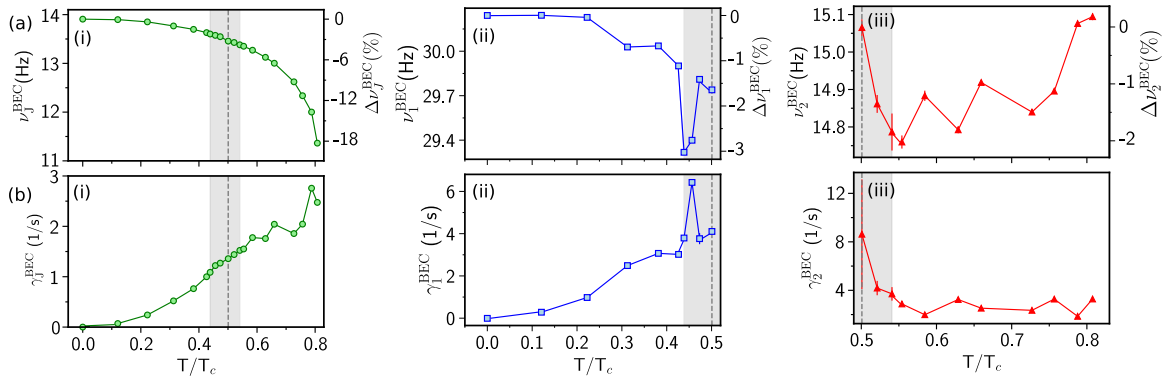

FIG. 4. Temperature dependence of (a) dominant frequencies, and (b) damping rates of the *condensate* component corresponding to the parameters of Fig. 3(a). These are shown for (i) the dominant, Josephson plasma, frequency $\nu_J^{\rm BEC}$ (plotted over the entire temperature range), and (ii),(iii) the other arising secondary frequencies over their respective regions of importance, i.e., (ii) $\nu_1^{\rm BEC}$, corresponding to the frequency around 30 Hz, and (iii) $\nu_2^{\rm BEC}$, corresponding to the frequency around 15 Hz (which is also the trap frequency along the x axis). The right axes of the frequency plots in (a) also show the % change of each frequency, which reveals a notable 18% lowering for $\nu_J^{\rm BEC}$, but a much weaker, few %, dependence for $\nu_1^{\rm BEC}$ and $\nu_2^{\rm BEC}$. (b) Josephson frequency damping rates [(i), $\gamma_J^{\rm BEC}$] increase monotonically with increasing temperature, and remain moderate over the entire probed regime, compared to $\gamma_1^{\rm BEC}$ and $\gamma_2^{\rm BEC}$, which, respectively, increase with increasing/decreasing temperature as they approach the crossover temperature $T \sim V_0/k_B$, labeled by the vertical dashed line.

of thermal cloud particles: as such, while the Josephson frequency is not significantly affected, its relative contribution decreases rapidly as the total population becomes more dependent on the increasing thermal contribution: at $T/T_c \sim 0.81$ the Josephson plasma mode contributes only about 20% of the total amplitude, while the phases of the two dominant contributions approach each other, indicating initial phase-locking. The increasing relative contribution of ν_2 with T, combined with the fact that the value of ν_2 is close to that of ν_J, causes the relative total population imbalance to exhibit beating between these two components with a beating frequency given by $f_{\rm beat} = |\nu_2^{\rm tot} - \nu_J^{\rm tot}|$: its inverse identifies a characteristic beating timescale, as indicated by an arrow in the $z^{\rm tot}(t)$ profile in Fig. 2(b). The beating frequency increases with higher T, as the $\nu_2^{\rm tot}$ value tends towards the trap frequency while the $\nu_J^{\rm tot}$ becomes even smaller. Moreover, we note that $f_{\rm beat}$ becomes larger even in the case of fixed T and larger barrier height as ν_J decreases with V_0 [31]. Thus the beating effect, which is a consequence of the effect of the thermal cloud, could be visible at shorter time ($\tau_{\rm beat} = 1/f_{\rm beat}$) for relatively large T in the case of fixed V_0 or for relatively large barrier height (but still not in the self-trapping regime) at fixed T.

More information on the properties of the dominant contributions to $z^{\rm BEC}(t)$ can be found in Fig. 4, which focuses on the dependence of the frequencies $\nu_{\rm J}$, ν_1, and ν_2 (top row) and corresponding damping rates (bottom row) as a function of scaled temperature T/T_c. We clearly see the monotonic decrease of $\nu_{\rm J}^{\rm BEC}$ over the entire temperature range probed, accompanied by a monotonic increase of the damping. For, e.g., $T \simeq 0.1T_c$, the damping extracted by the fit has a value broadly comparable to the one calculated from the Arrhenius-Kramers formula. Frequency ν_1 also decreases with increasing temperature, and its contribution damps at a faster rate than the $\nu_{\rm J}$-term, whereas ν_2 displays a less clear dependence and a corresponding large damping, which increases with decreasing temperature, eliminating that mode for $k_BT \ll V_0$: this somewhat counterintuitive behavior can be understood from the fact that at such lower temperatures, the thermal cloud cannot on its own move across the barrier, but can only do so mediated by the condensate, which drags it along. Since the analysis here focuses on behavior extracted from the condensate imbalance dynamics, and the small thermal component does not drag the condensate at low temperatures, it is understandable that no ν_2 contribution can be found at such low temperatures. These results are also confirmed by examining the discrete Fourier transform (DFT) of the condensate, thermal, and total population imbalance time series defined as

$$\tilde{z}(\nu_m) = \sum_{m=0}^{M-1} z_m e^{-i2\pi\nu_M m/M}, \tag{11}$$

where M is the number of samples, which are shown in Fig. 5 for (a) a low temperature, $T = 0.31T_c \ll V_0/k_B$, and (b) a much higher one, $T = 0.76T_c \gg V_0/k_B$. In the former case [Fig. 5(a)], the DFT shows a large amplitude peak at ν_J and a very small component at ν_1 which can be just resolved in the appropriate zoomed-in plot. As a consequence, even the thermal imbalance spectrum shows a component at the dominant condensate frequency ν_J. At high T instead, the thermal imbalance spectrum's main frequency is close to ν_2, i.e., around 15 Hz, which is different from the Josephson frequency ν_J. Moreover, the total imbalance (light green) has two main components, one close to the dominant condensate frequency and one close to the thermal imbalance main component, and due to their comparable relative contributions, the $z^{\rm tot}$ shows beating between these two frequencies at such high T.

C. $T > 0$ vortex-induced dissipative regime

We now consider the temperature dependence of the dynamics in the other dynamical regime of the junction, namely the vortex-induced dissipative regime [38,39], induced by an initial condensate population imbalance $z_0^{\rm BEC}$ which exceeds the corresponding critical value for plasma oscillations, i.e., $z_0^{\rm BEC} > z_{\rm cr}^{\rm BEC}$.

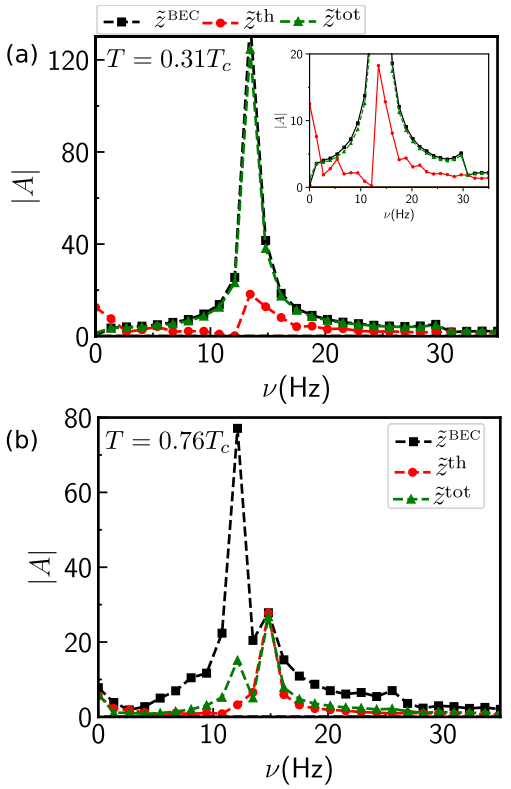

FIG. 5. The discrete Fourier transform (DFT) of the different population imbalance dynamics corresponding to the parameters of Fig. 3 ($z_0^{\rm BEC} < z_{\rm cr}^{\rm BEC}$) at two temperatures chosen such that (a) $T = 40$ nK $= 0.31T_c \ll V_0/k_B$, and (b) $T = 160$ nK $= 0.76T_c \gg V_0/k_B$. Depicted in each case are the contributions arising from the oscillating dynamics of the condensate $z_{\rm BEC}$(t) (black line), the thermal component $z_{\rm th}$(t) (red), and the total population imbalances $z_{\rm tot}$(t) (green). The y axis is the amplitude of the components of the DFT $|\tilde{z}|$, while the x axis is the frequency, exhibiting a numerical resolution of 1.3 Hz. The inset in (a) plots a zoomed-in version, which reveals the importance of the emerging ν_1 frequency across the different components analyzed.

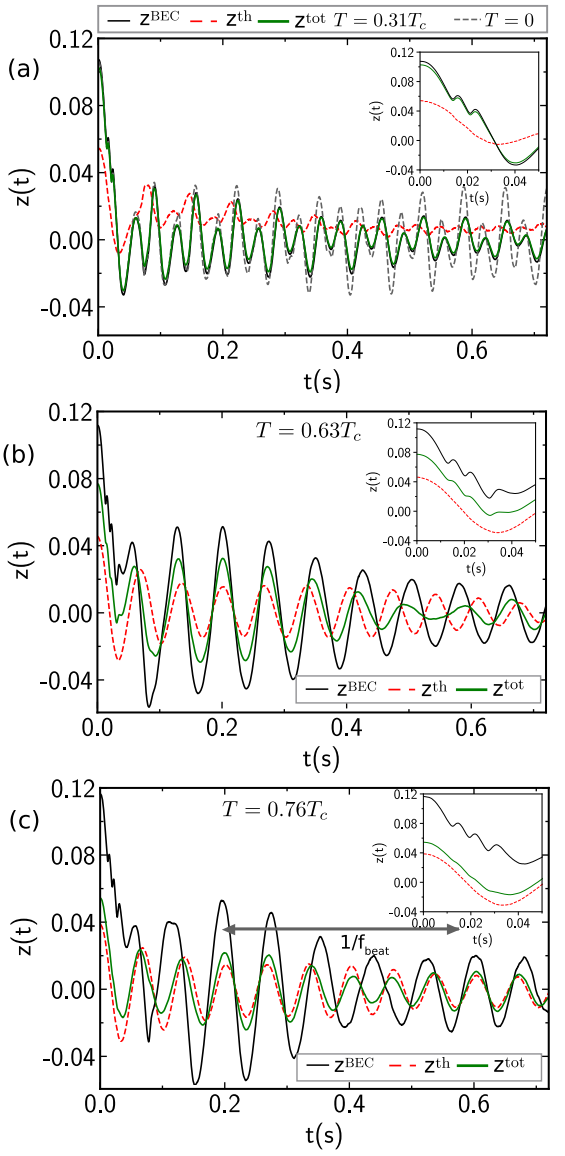

FIG. 6. Population imbalance oscillations for the condensate (black), thermal (red), and total (green) populations imbalance in the vortex-induced dissipative regime (i.e., for $z_0 = 0.11 > z_{\rm cr} = 0.08$) at different temperatures: (a) $T = 40$ nK $= 0.31T_c$, (b) $T = 100$ nK $= 0.63T_c$, and (c) $T = 160$ nK $= 0.76T_c$ for the case of a fixed condensate number $N^{\rm BEC} = 5.04 \times 10^4$ and a Gaussian barrier with $V_0 = 104\hbar\omega_x = 0.97\mu(T = 0)$ and $w = 3.8\xi$. Corresponding insets zoom into the early-time behavior to reveal the characteristic kinks in the *condensate* dynamics consistent with vortex generation; the importance of such dynamics in the total population imbalance clearly decreases with increasing temperature. The plots in (a) also show the pure superfluid ($T = 0$) results by a dashed gray line, revealing that the vortex ring generation process occurring at *early* times [inset to (a)] at low temperatures is practically indistinguishable from the corresponding $T = 0$ results, although the coupling to the thermal cloud induces more damping at *later* times. Beating emerges already for the case considered in (b), but becomes clearly pronounced (as indicated) on the probed timescale in (c).

The effect of temperature on such dynamics can be seen through characteristic (a) low-temperature, (b) intermediate-temperature, and (c) high-temperature plots of the corresponding condensate/thermal/total fractional population imbalances shown in Fig. 6.

At low temperatures where there is only a small thermal component, the total population imbalance is again dominated by the corresponding condensate one [Fig. 6(a)]; as such, they both reveal the characteristic early-time signature of vortex ring generation (black/green curves) through the two kinks in the early dynamical evolution of $z^{\rm BEC}(t)$, around 15 and 20 ms (see also zoomed-in plot). Although such vortex generation dynamics is practically indistinguishable from the pure superfluid $T = 0$ case (shown by dashed gray line), differences do arise in the longer-term evolution in the form of thermally induced damping. In this limit, the small thermal cloud dynamics is largely due to the condensate motion, with a small phase shift between them due to the repulsive interaction between condensate and thermal particles. At such low T, the thermal particles cannot pass over the barrier, so they exhibit incoherent tunneling. In the vortex-induced dissipative regime, the thermal imbalance oscillates around a nonzero value for longer time with respect to the Josephson

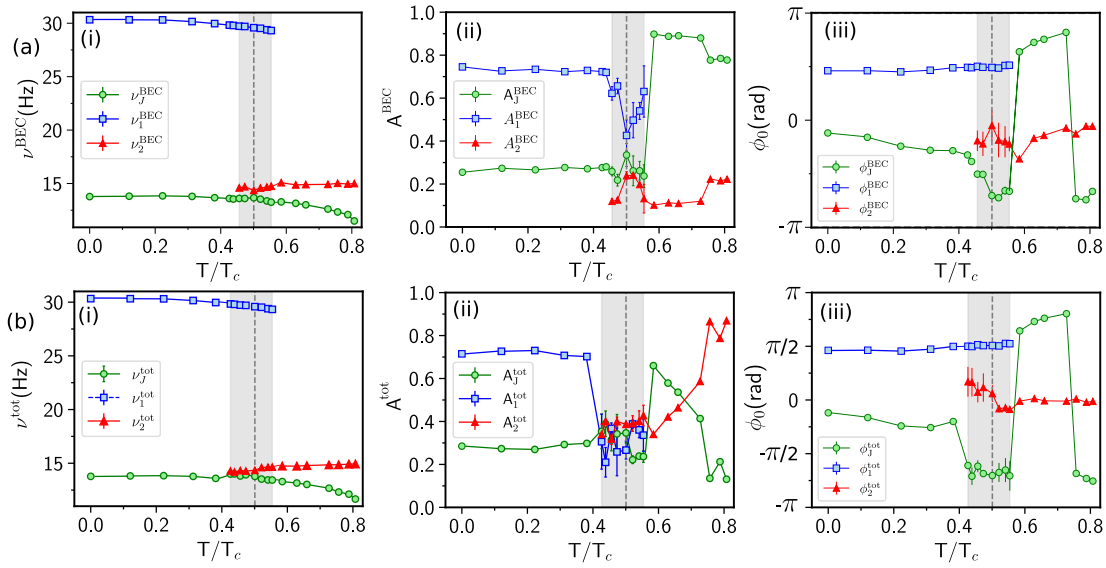

FIG. 7. Temperature dependence of oscillatory dynamics of (a) the condensate, and (b) the total population imbalance across a Josephson junction for a system of fixed condensate particle number, barrier amplitude $V_0/\mu \sim 0.97$, and initial condensate imbalance $z_0 > z_{\rm cr}$. Shown in each case are (i) the dominant oscillation frequencies, (ii) their relative amplitudes [extracted Eqs. (9) and (10)], and (iii) their corresponding initial phases [extracted through the fits of Eq. (9)] as a function of scaled temperature. This figure is closely related to the earlier Fig. 3, with all parameters/analysis/plotted lines having the same meaning, except that here $z_0 > z_{\rm cr}$, so that the superfluid is in the vortex-induced dissipative regime (as opposed to the Josephson dynamical regime considered in Fig. 3).

plasma regime. This could be understood by noticing that in the former, vortex rings are generated at the barrier position whose core is filled by the thermal cloud, i.e., it acts like a local "trapping" potential for the thermal particles, making it even harder for thermal particles to tunnel through the barrier. We note that for the chosen barrier height value, the vortex rings shrink within the barrier region without propagating [39]. After the shedding of the generated vortex rings, the condensate and therefore the total imbalance oscillate about a zero mean value at two frequencies (which will be shown to correspond to ν_J and ν_1), exhibiting damping.

As the temperature increases to values higher than the barrier [already visible in Fig. 6(b)], the thermal cloud (red line) exhibits its own dominant oscillatory decaying dynamics across the barrier. Interestingly, the condensate mode exhibits enhanced damping (due to the relative motion through the dynamical thermal cloud) and very quickly the condensate starts oscillating with a single dominant frequency, driven by the oscillating thermal component. The total imbalance profiles become more similar to the thermal one as the thermal fraction (i.e., as T) increases, and the presence of kinks during its initial decay becomes less visible in them with increasing T.

An interesting emerging feature here is the appearance of a third kink in the condensate population dynamics in the high-temperature region [see Fig. 6(c) and the corresponding inset], i.e., a third vortex ring is generated. We can trace this back to a small shift in $z^{\rm BEC}(t=0)$ with temperature: even though our temperature-dependent analysis fixed a linear tilted potential parameter ϵ and a condensate particle number, such a value of $z^{\rm BEC}(t=0)$ is indirectly affected by the fact that the thermal component dominates at the edges of the condensate density, thus slightly reducing (through mean-field repulsion) the condensate extent (and thus volume). We have indeed confirmed that if instead of fixing ϵ with varying temperatures we had explicitly chosen to fix $z^{\rm BEC}(t=0)$ in this $T>0$ case to exactly the same value as for $T=0$, the number of vortex rings being generated initially would be practically identical, even though differences would then emerge in the subsequent condensate dynamics. This is further discussed in Appendix E. Furthermore, we also note that the early-stage dynamics of the condensate imbalance (the initial decay) is slightly affected by the thermal particles, with the main dissipative mechanism being the generation/dynamics of vortex rings and associated sound waves.

At relatively high T [subplots (b) and (c)], the condensate and total imbalance show beating, whose frequency $f_{\rm beat}$ (period $\tau_{\rm beat}$) becomes larger (smaller) at higher T. An analysis (similar to Fig. 3) of the dominant frequencies, relative contributions, and initial phases as a function of temperature is shown in Fig. 7 for both (a) the condensate fractional population imbalance oscillations $z^{\rm BEC}(t)$ (top) and (b) the total population imbalance $z^{\rm tot}(t)$ (bottom). In the vortex-induced dissipative regime, the fit is performed after the initial decay.

Remarkably, the same three frequencies emerge, as found previously in the case of the Josephson regime both for the condensate [Fig. 7(a)(i)] and total imbalance [Fig. 7(b)(i)]. However, an important distinction becomes immediately apparent: although the dominant frequencies are the same as before, their relative contributions and initial relative phases of oscillations are not. Specifically, Figs. 7(a)(ii) and 7(b)(ii) show clearly that the Josephson plasma frequency term is no longer dominant at low temperatures, contributing less than 30% to the total amplitude at low temperatures in both condensate (a) and total imbalance (b). The generation of vortices and sound waves leads to significant interaction between the

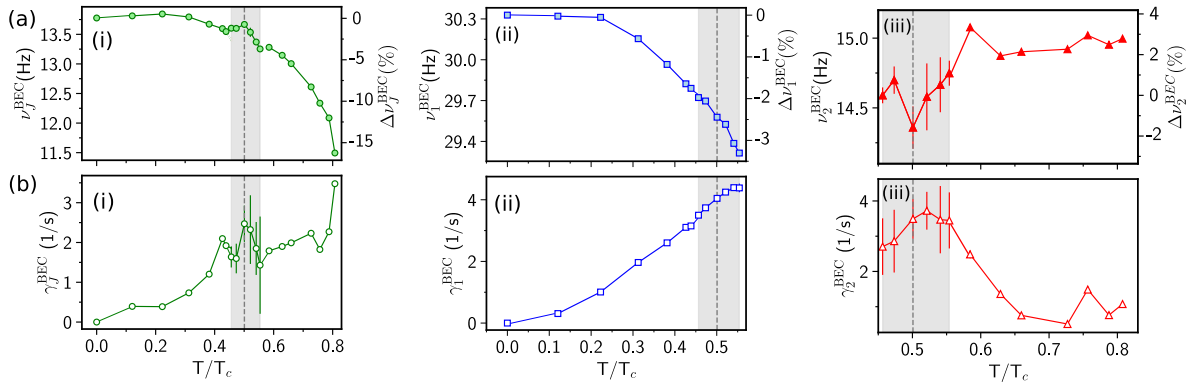

FIG. 8. Temperature dependence of (a) dominant frequencies, and (b) damping rates of the *condensate* component corresponding to the parameters of Fig. 7(a). These are shown for (i) the Josephson plasma, frequency $\nu_J^{\rm BEC}$ (plotted over the entire temperature range, but subdominant contribution for $T \lesssim V_0/k_B$), and (ii),(iii) the other arising frequencies over their respective regions of importance: these are (ii) $\nu_1^{\rm BEC}$, corresponding to the frequency around 30 Hz, which becomes dominant in the low-temperature regime due to the importance of acoustic emission during superflow dissipation, and (iii) $\nu_2^{\rm BEC}$, corresponding to the frequency around 15 Hz (which is also the trap frequency along the x axis). The right axes of the frequency plots in (a) also show the % change of each frequency, which reveals a notable 16% lowering for $\nu_J^{\rm BEC}$, but a much weaker, few %, dependence for $\nu_1^{\rm BEC}$ and $\nu_2^{\rm BEC}$. (b) Josephson frequency damping rates [(i), $\gamma_J^{\rm BEC}$] increase monotonically with increasing temperature (within error bars), while $\gamma_1^{\rm BEC}$ and $\gamma_2^{\rm BEC}$, respectively, increase with increasing/decreasing temperature as they approach the crossover temperature $T \sim V_0/k_B$, labeled by the vertical dashed line.

condensate and its excited sound waves, which affects the condensate imbalance spectrum even at $T = 0$. We note here that the frequency ν_1 is related to the presence of sound waves, as will be evident in the following section. Moreover, the initial phase of such a component is shifted around $\pi/2$ with respect to ϕ_J (at relatively low T). This would cause the presence of a dissipative component at the condensate current, which is finite even at $T = 0$, consistent with the results in Ref. [55].

Once again the behavior changes around $k_BT/V_0 \sim 1$, where the frequency ν_2 emerges, due to the oscillations of the increasing thermal cloud in the underlying axial harmonic trap. Interestingly, the primary role of the thermal cloud on the condensate motion initially appears to be to damp out the acoustic component with frequency ν_1: thus, perhaps somewhat counterintuitively, at higher temperatures the condensate reverts to single-frequency plasma oscillations, and so the Josephson contribution becomes more important, i.e., it becomes the dominant (∼80%) contribution to the condensate imbalance oscillations at higher temperatures.

The absolute phase difference between the Josephson and ν_1 contributions is now found to be reduced to about $\pi/2$ up until $k_BT/V_0 \sim 1$, a feature apparently also visible in the total population oscillations. In the latter case, the strong driving of the total particle number by the oscillating thermal cloud leads to approximately equal amplitudes for Josephson plasma and ν_2 contributions to the total population at $T = 0.59T_c$. Moreover, for even larger T the frequency $\nu_2^{\rm tot}$ [Fig. 7(b)(ii)], originating from the effect of the thermal cloud, becomes the dominant total imbalance component.

Looking into more detail at the three emerging frequencies, and the damping of the corresponding modes in Fig. 8, we note again the similar ν_J and ν_1 frequency dependence on T/T_c as found earlier in the Josephson plasma regime (Fig. 4); their values decrease with increasing T while the corresponding damping increases with T, with ν_1 being damped faster. Meanwhile, ν_2 frequency increases by tending to the x-axis trap frequency, while the corresponding damping decreases.

Figure 9 shows the DFT spectrum of the condensate, namely the total and the thermal imbalance for a low $T = 0.31T_c$ (a) and a high $T = 0.76T_c$ (b) temperature. At low T the thermal imbalance spectrum has the same components as the condensate one and the total imbalance spectrum is the same as the condensate one. At high T instead, the ν_1 frequency disappears from the spectrum and $\nu_2 \approx 15$ Hz appears. It originates from the dominant thermal imbalance dynamics, and manifests itself in both the condensate and the total imbalance spectrum. Moreover, at such high T the total imbalance spectrum is close to the thermal one instead.

Figure 10(i) shows "carpet plots" of the renormalized condensate density $\tilde{n}$ along the x-direction at (a) $T = 0$ and (b) $T = 0.63T_c$, with the corresponding population imbalance time evolution shown in Fig. 10(ii). In subplots (i), the density $\tilde{n}$ is evaluated by subtracting from the instantaneous density along the x axis its equilibrium value. In both cases, $V_0 \simeq \mu(T = 0)$ and thus the vortex rings disappear within the barrier and only the resulting sound waves propagate. Moreover, at relatively long-time evolution, sound waves are attenuated due to the presence of the thermal cloud. Thus, the disappearance of ν_1 from the condensate imbalance spectrum coincides with the total damping of sound modes, and this confirms the relation between ν_1 and sound waves. We note that the temperature T at which sound waves are damped due to the thermal particles depends on the value of V_0, and thus such an effect could also occur at smaller T for lower values of V_0, such that the thermal energy exceeds the barrier amplitude.[1]

[1]For example, for $V_0/\mu = 0.6$ the sound mode is damped already at $T = 60$ nK.

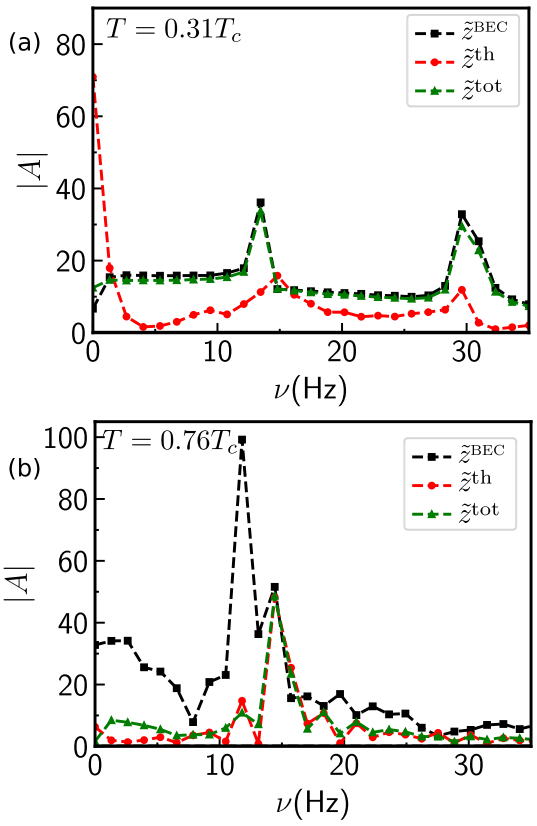

FIG. 9. The discrete Fourier transform (DFT) of the $z^{\rm BEC}(t)$ (black line), $z^{\rm th}(t)$ (red line), and $z^{\rm tot}(t)$ (green line) for $V_0 = 104\hbar\omega_x$ and $z_0^{\rm BEC} \simeq 0.11 > z_{\rm cr}^{\rm BEC}$ in the frequency domain for $T = 40$ nK $= 0.31T_c$ (a) and $T = 160$ nK $= 0.76T_c$ (b). The y axis is the amplitude of the components of the DFT $|\tilde{z}|$ while the x axis is the frequency. The DFT resolution is 1.3 Hz.

Our analysis so far has focused on the role of temperature in a system of fixed *condensate* particle number—and thus fixed condensate chemical potential μ—which amounts to a variable total particle number. Next, we consider the role of temperature at fixed *total* particle number.

IV. DYNAMICAL REGIMES AT A FIXED TOTAL NUMBER

When fixing instead the *total* number in the system, the effect of temperature is to decrease the condensate number with increasing temperature, due to the increasing presence of particles in the thermal cloud. This in turn implies that the chemical potential becomes temperature-dependent, $\mu(T)$, with a decreasing condensate particle number corresponding to a smaller $\mu(T)$ and smaller spatial extent, both of which significantly affect the system dynamics (see also Appendix A for details).

This is reflected by the density slices along the main axis (in the $y = z = 0$ transversal plane) for both the condensate and the thermal cloud at two different temperatures shown in Fig. 11(a) for fixed $N^{\rm tot} = 106\,000$. While the condensate density maxima decrease with T, the thermal cloud maxima instead (at the edges of the condensate) increase. Due to the presence of more thermal particles at the edges of the condensate and due to the repulsive interaction between the condensate and thermal particles, the condensate density extension along the x axis decreases. Moreover, the thermal cloud density at the barrier position increases, causing a type of repulsive potential at the center for the condensate particle, and as a consequence the condensate density at $x = 0$ decreases.

The tilted linear potential $-\epsilon x$ is initially taken to be the same at different T. Figure 11(b) shows the corresponding condensate and thermal imbalance temporal evolution for (i) $T = 0.41T_c$ and (ii) $T = 0.75T_c$.

Fixing the *total* number of particles while increasing the temperature has two important effects. First, the smaller BEC number implies that for the given imposed linear potential, the relative condensate population imbalance increases. Second, as $\mu(T)$ decreases with increasing T, the ratio $V_0/\mu(T)$ increases (for fixed V_0), which is known to decrease the value of the critical population imbalance (with all other parameters fixed) marking the transition between Josephson and vortex-induced dissipative regimes (as shown in Appendix C), even at the Gross-Pitaevskii level. Thus, for a given external linear potential, increasing temperature at a fixed total number can actually lead to a change in the dynamical regime of the condensate. This is clearly demonstrated in Fig. 11(b), showing the condensate population imbalance at $T = 0.41T_c$ (i) and at $T = 0.75T_c$ (ii): this clearly reveals both that $z_0^{\rm BEC}(T = 0.41T_c) < z_0^{\rm BEC}(T = 0.75T_c)$ and most significantly that the condensate population imbalance dynamics transitions from the Josephson regime at (i) $T = 0.41T_c$ to the vortex-induced dissipative regime at (ii) $T = 0.75T_c$.

Related questions of anticipated experimental relevance include the role of particle number, and whether one should be looking at condensate, or total, fractional population imbalance. For completeness, we also investigate the difference in the system behavior between the cases of fixing the condensate or the total initial population imbalance. These are shown, respectively, in Figs. 12(a) and 12(b). It demonstrates clearly that the transition across Josephson and dissipative regimes also occurs with changing temperature in the limit of fixed initial condensate or total population imbalance. The reason is that at two different temperatures, the ratio V_0/μ, which defines the system's dynamical regime, is different due to a different condensate number.

Moreover, we note that, as shown in Appendix C, the critical imbalance at which the system changes the dynamical regimes (defined from the condensate imbalance early-time dynamics) is already determined at the Gross-Pitaevskii level, with the thermal cloud having no significant effect at initial condensate imbalance evolution but strongly affecting its consequent dynamics (long-time evolution), as shown in the previous sections.

V. DISCUSSION

In this paper, we have analyzed for experimentally relevant conditions the role of thermal dissipation on the superfluid oscillations in the two dynamical regimes found in an elongated three-dimensional Josephson junction for barrier height close to the chemical potential and barrier width $w/\xi \simeq 4$, namely the Josephson "plasma" and the vortex-induced dissipative regime. The presence of the thermal cloud leads to relative

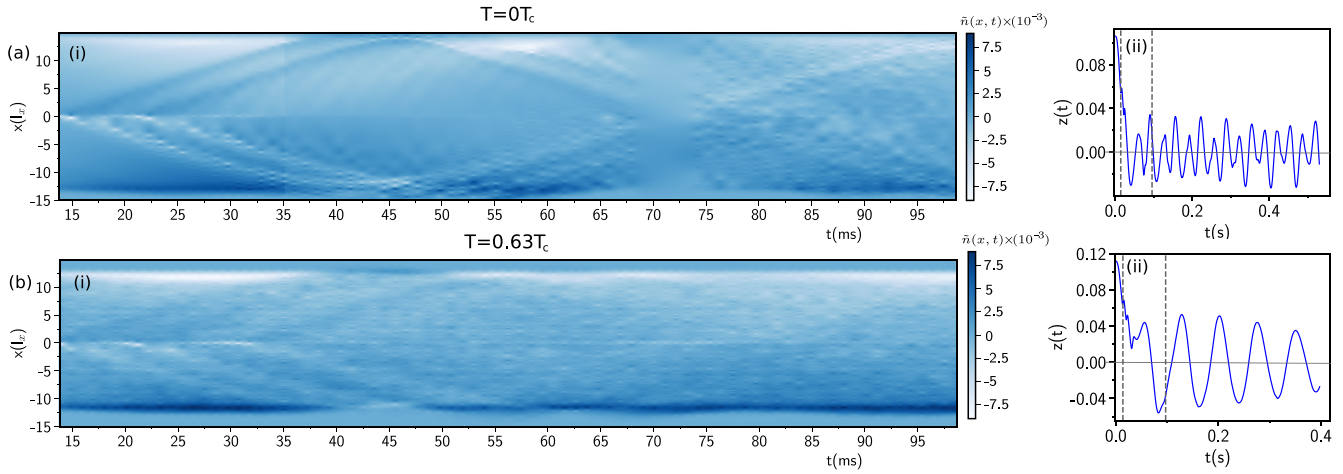

FIG. 10. Carpet plots of renormalized density $\tilde{n}(x,t)$ for $z_0^{\rm BEC} = 0.11$ (i) at $T = 0$ (a) and $T = 0.63T_c$ (b) and the corresponding condensate imbalance time evolution (ii) for $V_0 = 104\hbar\omega_x$. The vertical gray dashed lines in (ii) indicate the time interval of the carpet plots.

motion between the condensate and the thermal cloud and thus induces dissipative dynamics. In the Josephson plasma regime, this takes the form of a gradual damping of the condensate oscillations, with an associated decrease in the plasma frequency—with both effects becoming more pronounced with increasing temperature. While such a gradual decay mechanism is also at play in the dissipative regime, the short-time evolution in the latter regime exhibits much more drastic dynamics through the generation (and subsequent dynamics) of vortex rings and associated sound waves, which give a resistance to the junction that remains finite even at $T = 0$ [38,55], with the thermal cloud having only a comparably small effect in the early-stage dynamics. Thus, to better characterize the role of the thermal cloud on atomic population dynamics, this work has focused on the analysis of the long-time evolution of the superfluid dynamics.

Our analysis has revealed the emergence of three dominant frequencies across both probed regimes, with the relative importance of different modes depending on both dynamical regime and temperature.

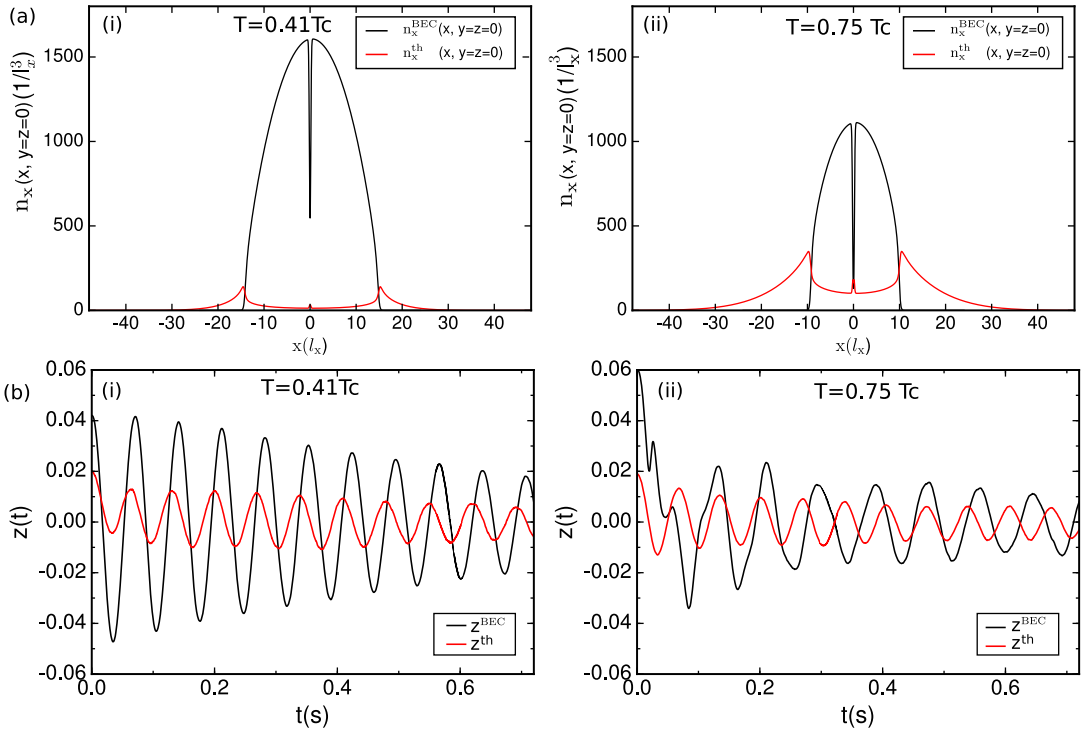

FIG. 11. (a) The condensate and the thermal cloud density profiles along the x axis ($y = z = 0$) at two different temperatures $T = 0.41T_c$ (i) and $T = 0.75T_c$ (ii). (b) The time evolution of the condensate and the thermal cloud imbalance for $T = 0.41T_c$ (i) and $T = 0.75T_c$ (ii). The total particle number is kept fixed at $N^{\rm tot} = 106\,000$. These data are also for fixed barrier height $V_0 = 104\hbar\omega_x$ and barrier shift ϵ along the x axis.

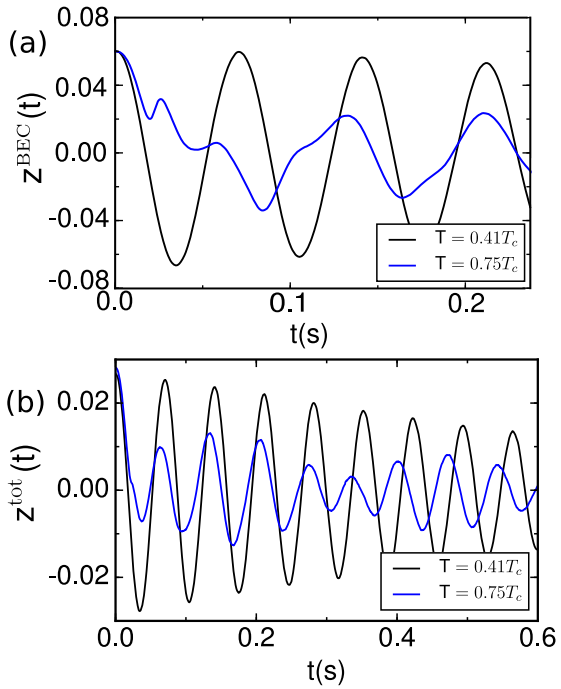

FIG. 12. The time evolution of the condensate imbalance (a) and of the total population imbalance (b) in the case when $z_0^{\rm BEC}$ and $z_0^{\rm tot}$ are fixed, respectively, at two different temperatures considered, $T = 0.41T_c$ (black line) and $T = 0.75T_c$ (blue line). The barrier height is kept fixed at $V_0 = 104\hbar\omega_x$ and fixed total number $N^{\rm tot} = 106\,000$.

First, as expected, our study has revealed a Josephson plasma frequency, ν_J, whose value was found to lie slightly below the axial trap frequency ν_x. While such a frequency dominates the low-temperature dynamical behavior in the Josephson regime, it was found (for the probed experimental parameters) to be subdominant in the dissipative regime. The damping of this plasma oscillation was found to increase monotonically with temperature (within error bars), with an associated decrease in ν_J of up to ∼18% across both Josephson and dissipative regimes.

At low temperatures $T \lesssim V_0/k_B$ the thermal cloud is relatively small, and is thus primarily driven by the condensate, with a characteristic phase lag. In this limit, we found an additional frequency that we labeled as ν_1. For our chosen parameters, this was found to be $\nu_1 \sim (2.1 - 2.2)\nu_J \sim 2\nu_x$. The presence of a second frequency at twice the Josephson frequency is expected to be found in the current-phase relation for barrier heights exceeding, but close to, the chemical potential, as already discussed in Refs. [38,55,61,64]. The importance of this mode (which can be interpreted as a phononlike mode) depends on the dynamical regime. In the Josephson plasma regime, this component was found to only play a small, secondary role in the condensate dynamics, leading to a component oscillating with a relative phase of $-\pi$ compared to the plasma oscillation component. Based on these considerations and knowing that the condensate current is found from the time derivative of the condensate imbalance, the frequency ν_1 is likely to be associated with the nondissipative second-order term in the current-phase relation "$\sin(2\Delta\phi)$" originating from the tunneling between condensate and noncondensate states, which at $T = 0$ are represented by phonon modes.

Interestingly, in the vortex-induced dissipative regime, the condensate dynamics could be "separated" into short- and long-time evolution; the former includes the time interval from the initial time until the time the vortex ring generation ceases (during which the condensate imbalance decays in time), while the latter includes the subsequent dynamics (during which the condensate imbalance oscillates around a zero mean value). The short-time evolution defines the maximum superfluid current flowing into the junction, and, for our geometry, this was previously shown [38] to depend on the terms coming from both the condensate-to-condensate state tunneling and the condensate-to-noncondensate tunneling; thus, the arising current-phase relation is sinusoidal of the form $I = I_c \sin(\Delta\phi) - J_1 \sin(2\Delta\phi)$. The present work instead focused on the long-time evolution, during which the condensate imbalance oscillates around zero value and the current-phase relation is linear. As $\nu_1 \approx 2\nu_J$ and it has an initial relative phase of $\pi/2$ with respect to ν_J, this could lead to the presence of a dissipative component of the form "$\cos(2\Delta\phi)$" in the current-phase relation (due to the presence of a finite chemical potential difference $\Delta\mu$ in our system [55]). However, it is very difficult to extract the importance of such a term directly from the current-phase relation. Specifically, at rather low temperatures, the emergence and propagation of sound waves (arising from the decay of the flow-induced generated vortices in the barrier region) lead to large current and phase fluctuations, which make the late-time extraction of a relative phase across the junction rather unreliable. In the opposite limit of high temperature ($T \gtrsim V_0/k_B$), the pronounced damping of the sound waves does lead to smoother phase profiles; however, in this limit the ν_1 frequency no longer contributes, being practically irrelevant for the condensate imbalance dynamics. This gives rise to the second frequency $\nu_2 \sim \nu_x$, consistent with dipole oscillations of the incoherent thermal cloud in the underlying harmonic trap, when the thermal cloud acquires sufficient energy to overcome the Gaussian barrier. In fact, in this case, the thermal cloud begins to drive the condensate dynamics, in stark contract to the low-temperature dynamics when the condensate is driving the thermal cloud.

Although the relevant frequencies of condensate oscillations beyond the plasma one, and the temperature dependence of their damping and relative phase difference, are similar across the Josephson plasma and phase-slip-induced dissipative regimes, we noted a significant difference in their relative importance at low temperatures $k_BT \lesssim V_0$. In particular, we found the ν_1 frequency component to dominate the dissipative regime condensate dynamics at sufficiently low temperatures $T \lesssim V_0/k_B$—presumably due to the abundance of sound-wave excitations during the phase slip and subsequent dynamics.

Notwithstanding the above comments, condensate dynamics on the high-temperature end are in both cases primarily dominated by plasma oscillations (with a significantly reduced frequency), even when the fraction of condensed particles is on the order of 10%. Once the dynamical thermal cloud is included, however, the total particle evolution exhibits a combination of self-driven plasma oscillations and thermal cloud oscillations in the trap, which lead to noticeable beating

in both condensate and total population imbalances, an effect that is within current experimental reach.

To keep a fixed condensate size and ratio of $V_0/\mu(T=0)$, our analysis was conducted for a fixed condensate number, thus implying a variable critical temperature for condensation. Our analysis was further extended to the case of a fixed total particle number, and we showed that having different condensate numbers at different T can cause the condensate or total population imbalance to be in a different dynamical regime due to different $N^{\rm BEC}$ and V_0/μ values.

VI. CONCLUSIONS

In brief, we characterized through state-of-the-art numerical simulations the temperature dependence and damping of dominant dynamical excitation modes of a finite-temperature superfluid across a thin Josephson junction, which supports a transition from plasma to dissipative phase-slip-induced regimes. Beyond the characterization of the plasma mode, we identified a further relevant low-temperature and high-temperature mode, distinguished by the ratio k_BT/V_0 of thermal to barrier energy; the thermal dynamics were shown to lead to damping of the condensate motion, with a new regime identified in which the (dominant) thermal cloud has enough energy to overcome the axial barrier and thus begins to drive the condensate out of phase, leading to beating in the condensate and/or total population dynamics. The additional frequency emerging in the low-temperature limit in the vortex-induced dissipative (or Josephson "plasma") regime was attributed to a second-order dissipative (nondissipative) term in the superfluid current, which derives from the tunneling between condensate to noncondensate states. Our findings, based on an established self-consistently coupled kinetic model, are within current experimental reach in ultracold superfluid junctions.

Data supporting this publication are openly available under an "Open Data Commons Open Database License" [82].

ACKNOWLEDGMENTS

We acknowledge discussions with Kean Loon Lee, I-Kang (Gary) Liu, Giacomo Roati, Francesco Scazza, and Matteo Zaccanti, and financial support from the QuantERA Project NAQUAS (EPSRC EP/R043434/1), and Qombs Project (FET Flagship on Quantum Technologies Grant No. 820419).

APPENDIX A: MODELING SCHEME DETAILS

Below, we give a brief summary of the kinetic model used in our work.

At finite temperature, the system wave function is written as the sum of a condensate wave function and a thermal cloud. The condensate wave-function evolution is found by solving the generalized Gross-Pitaevskii equation, which accounts for the thermal cloud mean field potential, $2gn^{\rm th}$ [69]:

$$i\hbar\frac{\partial\psi}{\partial t}=\left[-\frac{\hbar^2\nabla^2}{2M}+V_{\rm ext}+g(|\psi|^2+2n^{\rm th})\right]\psi, \qquad \text{(A1)}$$

with other symbols defined in the main text.

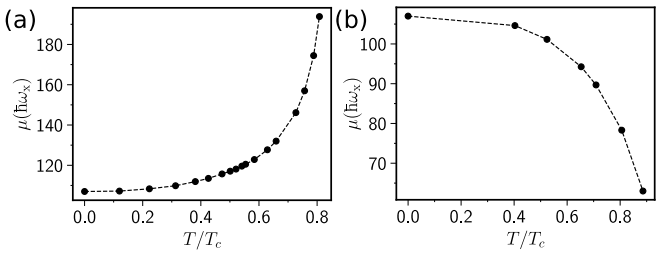

FIG. 13. The chemical potential as a function of the temperature T/T_c for fixed condensate number $N^{\rm BEC}\simeq 50\,400$ (a) and fixed total number $N^{\rm tot}=50\,400$ (b). Both plots are obtained for the same barrier height value $V_0=104\hbar\omega_x$.

To initiate the dynamics, we first obtain the equilibrium solution in a static potential including the harmonic trap, Gaussian barrier, and linear potential. The equilibrium condensate wave function ψ_0 is obtained self-consistently via

$$\mu(T)\psi_0=\left(-\frac{\hbar^2}{2M}\nabla^2+V_{\rm ext}+g\big(|\psi_0|^2+2n_0^{\rm th}\big)\right)\psi_0, \qquad \text{(A2)}$$

where $n_0^{\rm th}$ and $n_0^{\rm BEC}=|\psi_0|^2$ are the equilibrium thermal and condensate density, respectively, while $\mu(T)$ is the temperature-dependent system chemical potential accounting for the thermal cloud equilibrium mean-field potential. $V_{\rm ext}(\mathbf{r})$ is the trapping potential defined by Eq. (1). As described in [70–72], the initial thermal cloud density ansatz is based on a simple Gaussian for the required temperature. We then iterate those two equations self-consistently, until arriving at an equilibrium solution with the desired condensate, or total, particle number at each specified temperature.

The presence of the thermal cloud modifies the value of the chemical potential μ of the system, which takes into account also the mean-field potential of the thermal cloud. The main analysis in this paper is conducted at fixed condensate particle number $N^{\rm BEC}\simeq 5.04\times10^4$: for such parameters, the dependence of μ on the scaled temperature is shown in Fig. 13(a), which increases with T due to the increasing thermal fraction. In the opposite case of fixed total number, the temperature dependence of the chemical potential is shown in Fig. 13(b), revealing a decreasing dependence on temperature (due to the decreasing condensate number).

Changing temperature while keeping $N^{\rm BEC}$ fixed also changes $N^{\rm tot}$, and hence the corresponding noninteracting critical temperature $T_c=T_c(N)$. In our analysis, we specifically probe the temperature regime $T/T_c\lesssim 0.8$, for which the condensate fraction $N^{\rm BEC}/N^{\rm tot}\in[0.1,\ 1]$.

In the Hartree-Fock limit, and in the presence of an external potential, the energy of a particle becomes

$$\epsilon(\mathbf{r},t)=\frac{\mathbf{p}^2}{2m}+V_{\rm ext}(\mathbf{r})+2g[n^{\rm BEC}(\mathbf{r},t)+n^{\rm th}(\mathbf{r},t)]. \qquad \text{(A3)}$$

Thus the thermal particle feels a generalized effective potential:

$$V_{\rm eff}^{\rm th}(\mathbf{r},t)=V_{\rm ext}(\mathbf{r})+2g[n^{\rm BEC}(\mathbf{r},t)+n^{\rm th}(\mathbf{r},t)] \qquad \text{(A4)}$$

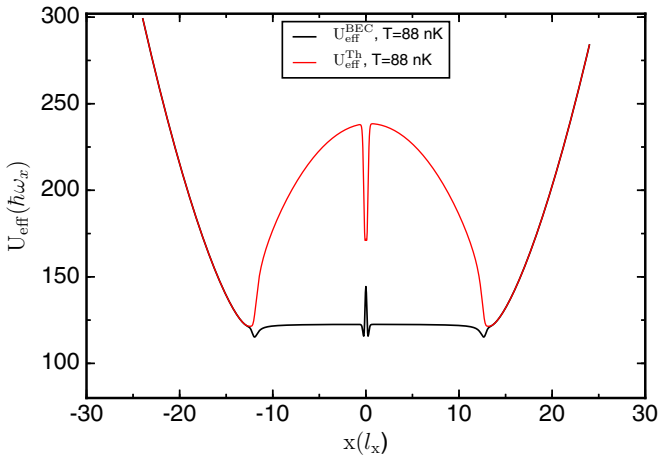

FIG. 14. The equilibrium effective potential felt by the condensate (black curve) and by the thermal cloud (red curve) at $T = 88$ nK $= 0.58T_c$ for $V_0 = 104\hbar\omega_x$.

while the condensate atoms feel an effective potential given by

$$V_{\rm eff}^{\rm BEC}(\mathbf{r},t) = V_{\rm ext} + g[n^{\rm BEC}(\mathbf{r},t) + 2n^{\rm th}(\mathbf{r},t)]. \tag{A5}$$

To seed the oscillatory dynamics, at $t = 0$, the linear potential is instantaneously removed, and the subsequent dynamics of all components are analyzed in detail. To account for thermal cloud dynamics, we solve this equation self-consistently with a collisionless Boltzmann equation for the thermal molecule phase-space distribution, f, obeying

$$\frac{\partial f}{\partial t} + \frac{\mathbf{p}}{M}\cdot\nabla_{\mathbf{r}} f - \nabla_{\mathbf{r}} V_{\rm eff}^{\rm th}\cdot\nabla_{\mathbf{p}} f = 0, \tag{A6}$$

where the thermal cloud density is defined by

$$n^{\rm th} = \frac{1}{(2\pi\hbar)^3}\int d\mathbf{p}\, f(\mathbf{p},\mathbf{r},t). \tag{A7}$$

Our model corresponds to the collisionless limit of the Zaremba-Nikuni-Griffin (ZNG) kinetic theory. References [69,71,72,74,77–79] show that this theoretical model successfully describes the collective modes, vortex dynamics, and evaporative cooling.

APPENDIX B: EQUILIBRIUM STATE

The equilibrium effective potential profile felt by the condensate and the thermal particle for a double-well potential are shown in Fig. 14 by black and red lines, respectively. Due to repulsive interaction between particles (i.e., $g > 0$), the thermal cloud feels a larger potential where the condensate density is larger, which means that the thermal particles would have lower density. This explains why the thermal cloud density has local maxima at the barrier position (where the condensate density is minimum) and at the edges of the condensate.

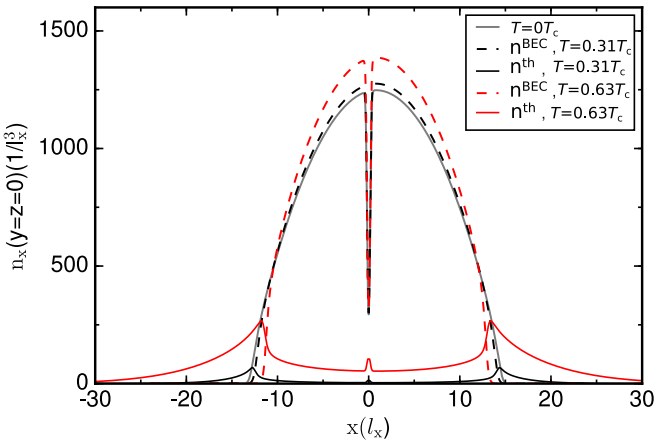

FIG. 15. The condensate density profile along the x direction ($y = z = 0$) for three different temperatures: $T = 0$ (gray line), $T = 40$ nK $= 0.31T_c$ (black dashed line), and $T = 100$ nK $= 0.63T_c$ (red dashed line) and the thermal cloud density shown as a black solid line for $T = 0.31T_c$ and as a red solid line for $T = 0.63T_c$. The barrier height is fixed at $V_0 = 104\hbar\omega_x$, $w/\xi \simeq 4$, and $N^{\rm BEC} \simeq 5.04\times10^4$.

For comparison, Fig. 15 shows the equilibrium condensate and thermal density along the x axis for $y = z = 0$ for three different temperatures: $T = 0$, $0.31T_c$, and $0.63T_c$. The numerical data are obtained for $V_0 = 104\hbar\omega_x \simeq \mu(T = 0)$ and in the presence of an initial imbalance. In all three case, the condensate number is kept fixed at $N^{\rm BEC} \simeq 5.04\times10^4$. We note that the presence of the thermal cloud at the edges of the condensate causes the condensate density to have a slightly smaller x axis extension with respect to the condensate at $T = 0$ where the thermal cloud is not present and thus a larger maximum density in order to keep the condensate number fixed. This effect is stronger at a higher temperature $T = 100$ nK $= 0.63T_c$.

APPENDIX C: THE CRITICAL IMBALANCE

Based on the short-time evolution of the condensate population imbalance, a critical value of initial imbalance is found $z_{\rm cr}^{\rm BEC}$, which is defined as the value of initial imbalance where only one phase-slippage occurs and thus only one vortex ring is generated. Figure 16(a) shows the profile of the critical imbalance as a function of the barrier height value, and 16(b)

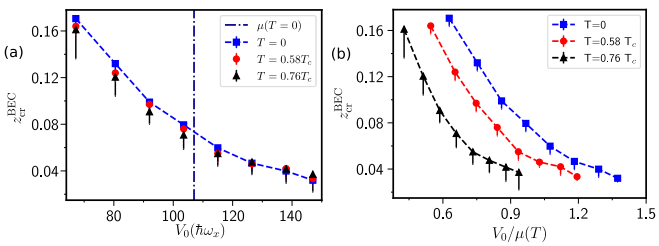

FIG. 16. The critical condensate initial imbalance at $T = 0$, $T = 0.58T_c$, and $T = 160$ nK $= 0.76T_c$ as a function of V_0 (a) and $V_0/\mu(T)$ (b). These data are for fixed condensate number when comparing $T = 0$ and finite T results. The dashed line in (a) indicates the chemical potential at $T = 0$.

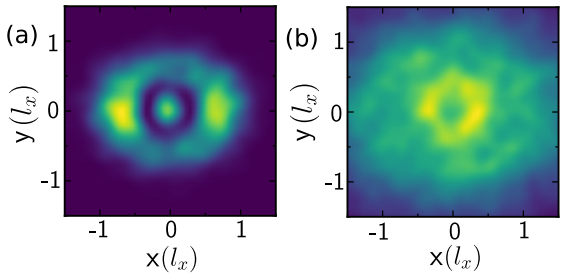

FIG. 17. The condensate (a) and thermal cloud density (b) along the yz plane and in the presence of a vortex ring. This data are for $T = 0.58T_c$ and for $V_0/\mu(T = 0) = 0.6$.

shows the corresponding plot with the barrier height scaled to the chemical potential at finite T. In these plots, the condensate number is fixed at $N^{\rm BEC} \simeq 5.04 \times 10^4$, which means $N^{\rm tot}$ varies with T. We first note that as T increases, and for fixed V_0 [i.e., $V_0/\mu(T = 0)$], the critical imbalance is not affected by the presence of the thermal cloud. If instead the $V_0/\mu(T)$ is fixed, the critical condensate imbalance at finite T differs from its value at $T = 0$, and this difference is larger for larger values of T/T_c. In fact, at $T = 0.3T_c$ as in our previous studies where the condensate fraction is 90% and within numerical error bars, $z_{\rm cr}^{\rm BEC}(T = 0.3T_c) \simeq z_{\rm cr}^{\rm BEC}(T = 0)$ for the same $V_0/\mu(T)$. Moreover, as T increases, $z_{\rm cr}^{\rm BEC}$ shifts more from its corresponding $T = 0$ value, thus being smaller for the same value $V_0/\mu(T)$.

APPENDIX D: THE VORTEX RING AT FINITE T

In our 3D geometry, every time the superfluid velocity exceeds a critical value, vortex rings are generated. The vortex ring has a core that is characterized by a vanishing condensate density as visible in Fig. 17(a). At finite temperature, the repulsive interactions between the condensate and thermal cloud densities can lead the vortex ring core to becomes itself populated by the thermal cloud, as shown in Fig. 17(b).

APPENDIX E: THE ROLE OF THE THERMAL CLOUD ON INITIAL CONDENSATE IMBALANCE

As we showed in the main text (Sec. III C and Fig. 6), for $T \gtrsim 0.58T_c$ and in the vortex-induced dissipative regime, there is a third "dip" (or kink) in the initial decay of the condensate population imbalance, corresponding to the generation of an additional vortex ring. We also noted that the concentration of the thermal cloud at the condensate edges and at the barrier induces a small shift in the condensate initial imbalance, which slightly increases with temperature. The first question is whether the new shifted $z_0^{\rm BEC}$ would have been large enough at $T = 0$ to cause the transition to a regime when another phase slippage happens, or if it comes from the thermal induced fluctuations of the phase. The second question is related to the reason why at $T = 0.58T_c$ the $\nu_1^{\rm BEC}$ "disappears" from the spectrum of the condensate imbalance when for $T < 0.58T_c$ its contribution is large, around 60%.

To answer such questions, we consider also the case when the initial condensate imbalance is fixed between the cases of $T = 0$ and the selected $T = 0.66T_c$, instead of fixing ϵ of the lineal potential $-\epsilon x$. Figure 18 shows the condensate population imbalance for $T = 0$ and $T = 110$ nK $= 0.66T_c$ for two slightly different initial population imbalances $z_0 = 0.106$ and 0.113. These values of z_0 have been chosen such that the first one produces the same barrier shift as $T = 0.66T_c$, while the second one is exactly equal to the initial condensate imbalance $z_0^{\rm BEC}$ at $T = 0.66T_c$.

We observe that at $T = 0$, the condensate population imbalance for $z_0 = 0.113$, which is equal to the initial condensate imbalance at $T = 0.66T_c$, presents a third "dip," indicated by the white rectangle in the zoomed-in profile in Fig. 18(b). Thus this analysis explains the origin of the third generated vortex ring (for $V_0 = 104\hbar\omega_x$). We note that the initial decay of the condensate imbalance is similar for ($T = 0$, $z_0 = 0.113$) and $T = 0.66T_c$. Furthermore, the temporal profile of the population imbalance at $T = 0$, after the initial decay, shows different features for $z_0 = 0.113$ with respect to $z_0 = 0.106$. In particular, in the first case the frequency near 30 Hz, i.e., the $\nu_1^{\rm BEC}$ frequency, is less important than the Josephson "plasma" frequency. As we have shown previously, the opposite happens for $z_0 = 0.106$, where the ν_1 is the dominant frequency. Thus this answers our second question. Moreover, from Fig. 18 we observe also that the long-time evolution differs between ($T = 0$, $z_0 = 0.113$) and $T = 0.66T_c$, i.e., for the same initial condensate imbalance between $T = 0$ and $0.66T_c$, due to the presence of a significant thermal fraction at this temperature that damps the second-order term.

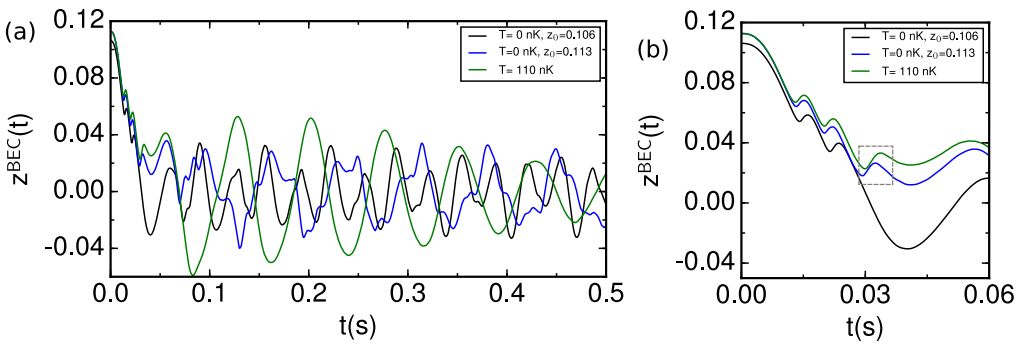

FIG. 18. (a) The condensate population imbalance time evolution at $T = 0$ and for two slightly different z_0 and at $T = 110$ nK $= 0.66T_c$ with a zoomed-in corresponding profile shown in (b). The data are for $V_0 = 104\hbar\omega_x$ and fixed $N^{\rm BEC} \simeq 50\,400$.

[1] B. D. Josephson, Possible new effects in superconductive tunnelling, Phys. Lett. **1**, 251 (1962).

[2] P. W. Anderson and J. M. Rowell, Probable Observation of the Josephson Superconducting Tunneling Effect, Phys. Rev. Lett. **10**, 230 (1963).

[3] A. Barone and G. Paterno, *Physics and Applications of the Josephson Effect* (Wiley, New York, 1982).

[4] O. Avenel and E. Varoquaux, Josephson Effect and Quantum Phase Slippage in Superfluids, Phys. Rev. Lett. **60**, 416 (1988).

[5] J. C. Davis and R. E. Packard, Superfluid ^{3}He josephson weak links, Rev. Mod. Phys. **74**, 741 (2002).

[6] Y. Sato, E. Hoskinson, and R. E. Packard, Josephson effects in superfluid helium, in *Fundamentals and Frontiers of the Josephson Effect*, edited by F. Tafuri, Vol. 286 (Springer, Cham, 2019).

[7] E. Hoskinson, Y. Sato, I. Hahn, and R. E. Packard, Transition from phase slips to the josephson effect in a superfluid ^{4}He weak link, Nat. Phys. **2**, 23 (2006).

[8] B. P. Anderson and M. Kasevich, Macroscopic quantum interference from atomic tunnel arrays, Science **282**, 1686 (1998).

[9] F. S. Cataliotti, S. Burger, C. Fort, P. Maddaloni, F. Minardi, A. Trombettoni, A. Smerzi, and M. Inguscio, Josephson junction arrays with Bose-Einstein condensates, Science **293**, 843 (2001).

[10] M. Albiez, R. Gati, J. Fölling, S. Hunsmann, M. Cristiani, and M. K. Oberthaler, Direct Observation of Tunneling and Nonlinear Self-Trapping in a Single Bosonic Josephson Junction, Phys. Rev. Lett. **95**, 010402 (2005).

[11] T. Anker, M. Albiez, R. Gati, S. Hunsmann, B. Eiermann, A. Trombettoni, and M. K. Oberthaler, Nonlinear Self-Trapping of Matter Waves in Periodic Potentials, Phys. Rev. Lett. **94**, 020403 (2005).

[12] T. Schumm, S. Hofferberth, L. M. Andersson, S. Wildermuth, S. Groth, I. Bar-Joseph, J. Schmiedmayer, and P. Krüger, Matter-wave interferometry in a double well on an atom chip, Nat. Phys. **1**, 57 (2005).

[13] Y. Shin, M. Saba, T. A. Pasquini, W. Ketterle, D. E. Pritchard, and A. E. Leanhardt, Atom Interferometry with Bose-Einstein Condensates in a Double-Well Potential, Phys. Rev. Lett. **92**, 050405 (2004).

[14] S. Levy, E. Lahoud, I. Shomroni, and J. Steinhauer, The a.c. and d.c. Josephson effects in a Bose–Einstein condensate, Nature (London) **449**, 579 (2007).

[15] G. Spagnolli, G. Semeghini, L. Masi, G. Ferioli, A. Trenkwalder, S. Coop, M. Landini, L. Pezzè, G. Modugno, M. Inguscio, A. Smerzi, and M. Fattori, Crossing Over from Attractive to Repulsive Interactions in a Tunneling Bosonic Josephson Junction, Phys. Rev. Lett. **118**, 230403 (2017).

[16] L. J. LeBlanc, A. B. Bardon, J. McKeever, M. H. T. Extavour, D. Jervis, J. H. Thywissen, F. Piazza, and A. Smerzi, Dynamics of a Tunable Superfluid Junction, Phys. Rev. Lett. **106**, 025302 (2011).

[17] G. Valtolina, A. Burchianti, A. Amico, E. Neri, K. Xhani, J. A. Seman, A. Trombettoni, A. Smerzi, M. Zaccanti, M. Inguscio, and G. Roati, Josephson effect in fermionic superfluids across the BEC-BCS crossover, Science **350**, 1505 (2015).

[18] A. Burchianti, F. Scazza, A. Amico, G. Valtolina, J. A. Seman, C. Fort, M. Zaccanti, M. Inguscio, and G. Roati, Connecting Dissipation and Phase Slips in a Josephson Junction between Fermionic Superfluids, Phys. Rev. Lett. **120**, 025302 (2018).

[19] W. J. Kwon, G. Del Pace, R. Panza, M. Inguscio, W. Zwerger, M. Zaccanti, F. Scazza, and G. Roati, Strongly correlated superfluid order parameters from dc Josephson supercurrents, Science **369**, 84 (2020).

[20] N. Luick, L. Sobirey, M. Bohlen, V. P. Singh, L. Mathey, T. Lompe, and H. Moritz, An ideal Josephson junction in an ultracold two-dimensional fermi gas, Science **369**, 89 (2020).

[21] G. Del Pace, W. J. Kwon, M. Zaccanti, G. Roati, and F. Scazza, Tunneling Transport of Unitary Fermions across the Superfluid Transition, Phys. Rev. Lett. **126**, 055301 (2021).

[22] K. G. Lagoudakis, B. Pietka, M. Wouters, R. André, and B. Deveaud-Plédran, Coherent Oscillations in an Exciton-Polariton Josephson Junction, Phys. Rev. Lett. **105**, 120403 (2010).

[23] A. F. Adiyatullin, M. D. Anderson, H. Flayac, M. T. Portella-Oberli, F. Jabeen, C. Ouellet-Plamondon, G. C. Sallen, and B. Deveaud, Periodic squeezing in a polariton Josephson junction, Nat. Commun. **8**, 1329 (2017).

[24] M. Edwards, Atom squid, Nat. Phys. **9**, 68 (2013).

[25] C. Ryu, P. W. Blackburn, A. A. Blinova, and M. G. Boshier, Experimental Realization of Josephson Junctions for an Atom SQUID, Phys. Rev. Lett. **111**, 205301 (2013).

[26] C. Ryu, E. C. Samson, and M. G. Boshier, Quantum interference of currents in an atomtronic squid, Nat. Commun. **11**, 3338 (2020).

[27] L. Amico, M. Boshier, G. Birkl, A. Minguzzi, C. Miniatura, L.-C. Kwek, D. Aghamalyan, V. Ahufinger, D. Anderson, N. Andrei, A. S. Arnold, M. Baker, T. A. Bell, T. Bland, J. P. Brantut, D. Cassettari, W. J. Chetcuti, F. Chevy, R. Citro, S. De Palo *et al.*, Roadmap on atomtronics: State of the art and perspective, AVS Quantum Sci. **3**, 039201 (2021).

[28] G. Gauthier, S. S. Szigeti, M. T. Reeves, M. Baker, T. A. Bell, H. Rubinsztein-Dunlop, M. J. Davis, and T. W. Neely, Quantitative Acoustic Models for Superfluid Circuits, Phys. Rev. Lett. **123**, 260402 (2019).

[29] A. Smerzi, S. Fantoni, S. Giovanazzi, and S. R. Shenoy, Quantum Coherent Atomic Tunneling between Two Trapped Bose-Einstein Condensates, Phys. Rev. Lett. **79**, 4950 (1997).

[30] S. Raghavan, A. Smerzi, S. Fantoni, and S. R. Shenoy, Coherent oscillations between two weakly coupled Bose-Einstein condensates: Josephson effects, π oscillations, and macroscopic quantum self-trapping, Phys. Rev. A **59**, 620 (1999).

[31] I. Zapata, F. Sols, and A. J. Leggett, Josephson effect between trapped Bose-Einstein condensates, Phys. Rev. A **57**, R28 (1998).

[32] E. Sakellari, N. P. Proukakis, M. Leadbeater, and C. S. Adams, Josephson tunnelling of a phase-imprinted bose–einstein condensate in a time-dependent double-well potential, New J. Phys. **6**, 42 (2004).

[33] M. Abad, M. Guilleumas, R. Mayol, F. Piazza, D. M. Jezek, and A. Smerzi, Phase slips and vortex dynamics in Josephson oscillations between Bose-Einstein condensates, Europhys. Lett. **109**, 40005 (2015).

[34] F. Pascucci and L. Salasnich, Josephson effect with superfluid fermions in the two-dimensional BCS-BEC crossover, Phys. Rev. A **102**, 013325 (2020).

[35] A. Spuntarelli, P. Pieri, and G. C. Strinati, Josephson effect throughout the BCS-BEC Crossover, Phys. Rev. Lett. **99**, 040401 (2007).

[36] J. Polo, R. Dubessy, P. Pedri, H. Perrin, and A. Minguzzi, Oscillations and Decay of Superfluid Currents in a One-Dimensional Bose Gas on a Ring, Phys. Rev. Lett. **123**, 195301 (2019).

[37] A. K. Saha and R. Dubessy, Dynamical phase diagram of a one-dimensional Bose gas in a box with a tunable weak link: From Bose-Josephson oscillations to shock waves, Phys. Rev. A **104**, 023316 (2021).

[38] K. Xhani, E. Neri, L. Galantucci, F. Scazza, A. Burchianti, K.-L. Lee, C. F. Barenghi, A. Trombettoni, M. Inguscio, M. Zaccanti, G. Roati, and N. P. Proukakis, Critical Transport and Vortex Dynamics in a Thin Atomic Josephson Junction, Phys. Rev. Lett. **124**, 045301 (2020).

[39] K. Xhani, L. Galantucci, C. F. Barenghi, G. Roati, A. Trombettoni, and N. P. Proukakis, Dynamical phase diagram of ultracold Josephson junctions, New J. Phys. **22**, 123006 (2020).

[40] F. Jendrzejewski, S. Eckel, N. Murray, C. Lanier, M. Edwards, C. J. Lobb, and G. K. Campbell, Resistive Flow in a Weakly Interacting Bose-Einstein Condensate, Phys. Rev. Lett. **113**, 045305 (2014).

[41] S. Eckel, J. G. Lee, F. Jendrzejewski, C. J. Lobb, G. K. Campbell, and W. T. Hill, Contact resistance and phase slips in mesoscopic superfluid-atom transport, Phys. Rev. A **93**, 063619 (2016).

[42] F. Piazza, L. A. Collins, and A. Smerzi, Instability and vortex ring dynamics in a three-dimensional superfluid flow through a constriction, New J. Phys. **13**, 043008 (2011).

[43] A. Griffin, S. Nazarenko, and D. Proment, Breaking of Josephson junction oscillations and onset of quantum turbulence in Bose–Einstein condensates, J. Phys. A **53**, 175701 (2020).

[44] B. I. Halperin, G. Refael, and E. Demler, Resistance in superconductors, Int. J. Mod. Phys. B **24**, 4039 (2010).

[45] Y. Chen, Y.-H. Lin, S. D. Snyder, A. M. Goldman, and A. Kamenev, Dissipative superconducting state of non-equilibrium nanowires, Nat. Phys. **10**, 567 (2014).

[46] K. C. Wright, R. B. Blakestad, C. J. Lobb, W. D. Phillips, and G. K. Campbell, Driving Phase Slips in a Superfluid Atom Circuit with a Rotating Weak Link, Phys. Rev. Lett. **110**, 025302 (2013).

[47] K. Snizhko, K. Isaieva, Y. Kuriatnikov, Y. Bidasyuk, S. Vilchinskii, and A. Yakimenko, Stochastic phase slips in toroidal Bose-Einstein condensates, Phys. Rev. A **94**, 063642 (2016).

[48] A. Smerzi, A. Trombettoni, T. Lopez-Arias, C. Fort, P. Maddaloni, F. Minardi, and M. Inguscio, Macroscopic oscillations between two weakly coupled Bose-Einstein condensates, Eur. Phys. J. B **31**, 457 (2003).

[49] A. Smerzi and A. Trombettoni, Nonlinear tight-binding approximation for Bose-Einstein condensates in a lattice, Phys. Rev. A **68**, 023613 (2003).

[50] S. Raghavan, A. Smerzi, and V. M. Kenkre, Transitions in coherent oscillations between two trapped Bose-Einstein condensates, Phys. Rev. A **60**, R1787 (1999).

[51] I. Marino, S. Raghavan, S. Fantoni, S. R. Shenoy, and A. Smerzi, Bose-condensate tunneling dynamics: Momentum-shortened pendulum with damping, Phys. Rev. A **60**, 487 (1999).

[52] E. Sakellari, M. Leadbeater, N. J. Kylstra, and C. S. Adams, Josephson spectroscopy of a dilute Bose-Einstein condensate in a double-well potential, Phys. Rev. A **66**, 033612 (2002).

[53] P. Zou and F. Dalfovo, Josephson oscillations and self-trapping of superfluid fermions in a double-well potential, J. Low Temp. Phys. **177**, 240 (2014).

[54] Y. M. Bidasyuk, M. Weyrauch, M. Momme, and O. O. Prikhodko, Finite-temperature dynamics of a bosonic Josephson junction, J. Phys. B **51**, 205301 (2018).

[55] F. Meier and W. Zwerger, Josephson tunneling between weakly interacting Bose-Einstein condensates, Phys. Rev. A **64**, 033610 (2001).

[56] V. Piselli, S. Simonucci, and G. Calvanese Strinati, Josephson effect at finite temperature along the BCS-BEC crossover, Phys. Rev. B **102**, 144517 (2020).

[57] R. Gati, B. Hemmerling, J. Fölling, M. Albiez, and M. K. Oberthaler, Noise Thermometry with Two Weakly Coupled Bose-Einstein Condensates, Phys. Rev. Lett. **96**, 130404 (2006).

[58] A. Imamoğlu, M. Lewenstein, and L. You, Inhibition of Coherence in Trapped Bose-Einstein Condensates, Phys. Rev. Lett. **78**, 2511 (1997).

[59] R. Franzosi, V. Penna, and R. Zechina, Quantum dynamics of coupled bosonic wells within the Bose–hubbard picture, Int. J. Mod. Phys. B **14**, 943 (2000).

[60] G. J. Milburn, J. Corney, E. M. Wright, and D. F. Walls, Quantum dynamics of an atomic Bose-Einstein condensate in a double-well potential, Phys. Rev. A **55**, 4318 (1997).

[61] V. P. Singh, N. Luick, L. Sobirey, and L. Mathey, Josephson junction dynamics in a two-dimensional ultracold Bose gas, Phys. Rev. Research **2**, 033298 (2020).

[62] J. Polo, V. Ahufinger, F. W. J. Hekking, and A. Minguzzi, Damping of Josephson Oscillations in Strongly Correlated One-Dimensional Atomic Gases, Phys. Rev. Lett. **121**, 090404 (2018).

[63] F. Dalfovo, S. Giorgini, L. P. Pitaevskii, and S. Stringari, Theory of Bose-Einstein condensation in trapped gases, Rev. Mod. Phys. **71**, 463 (1999).

[64] M. Zaccanti and W. Zwerger, Critical Josephson current in BCS-BEC–crossover superfluids, Phys. Rev. A **100**, 063601 (2019).

[65] Y. M. Bidasyuk, O. O. Prikhodko, and M. Weyrauch, Phonon-Josephson resonances in atomtronic circuits, Phys. Rev. A **94**, 033603 (2016).

[66] S. Martínez-Garaot, G. Pettini, and M. Modugno, Nonlinear mixing of Bogoliubov modes in a bosonic Josephson junction, Phys. Rev. A **98**, 043624 (2018).

[67] E. Goldobin, D. Koelle, R. Kleiner, and A. Buzdin, Josephson junctions with second harmonic in the current-phase relation: Properties of φ junctions, Phys. Rev. B **76**, 224523 (2007).

[68] S. Uchino and J.-P. Brantut, Bosonic superfluid transport in a quantum point contact, Phys. Rev. Research **2**, 023284 (2020).

[69] A. Griffin, T. Nikuni, and E. Zaremba, *Bose-Condensed Gases at Finite Temperatures* (Cambridge University Press, Cambridge, 2009).

[70] B. Jackson and E. Zaremba, Modeling Bose-Einstein condensed gases at finite temperatures with n-body simulations, Phys. Rev. A **66**, 033606 (2002).

[71] N. P. Proukakis and B. Jackson, Finite-temperature models of Bose–Einstein condensation, J. Phys. B **41**, 203002 (2008).

[72] *Quantum Gases: Finite Temperature and Non-Equilibrium Dynamics*, edited by N. Proukakis, S. Gardiner, M. Davis, and M. Szymańska (Imperial College, London, 2013).

[73] M. J. Bijlsma, E. Zaremba, and H. T. C. Stoof, Condensate growth in trapped Bose gases, Phys. Rev. A **62**, 063609 (2000).

[74] B. Jackson and E. Zaremba, Quadrupole Collective Modes in Trapped Finite-Temperature Bose-Einstein Condensates, Phys. Rev. Lett. **88**, 180402 (2002).

[75] B. Jackson and E. Zaremba, Finite-Temperature Simulations of the Scissors Mode in Bose-Einstein Condensed Gases, Phys. Rev. Lett. **87**, 100404 (2001).

[76] B. Jackson, N. P. Proukakis, and C. F. Barenghi, Dark-soliton dynamics in Bose-Einstein condensates at finite temperature, Phys. Rev. A **75**, 051601(R) (2007).

[77] B. Jackson, N. P. Proukakis, C. F. Barenghi, and E. Zaremba, Finite-temperature vortex dynamics in Bose-Einstein condensates, Phys. Rev. A **79**, 053615 (2009).

[78] A. J. Allen, E. Zaremba, C. F. Barenghi, and N. P. Proukakis, Observable vortex properties in finite-temperature Bose gases, Phys. Rev. A **87**, 013630 (2013).

[79] A. J. Allen, S. Zuccher, M. Caliari, N. P. Proukakis, N. G. Parker, and C. F. Barenghi, Vortex reconnections in atomic condensates at finite temperature, Phys. Rev. A **90**, 013601 (2014).

[80] A. Burchianti, C. Fort, and M. Modugno, Josephson plasma oscillations and the Gross-Pitaevskii equation: Bogoliubov approach versus two-mode model, Phys. Rev. A **95**, 023627 (2017).

[81] G.-S. Paraoanu, S. Kohler, F. Sols, and A. J. Leggett, The Josephson plasmon as a bogoliubov quasiparticle, J. Phys. B **34**, 4689 (2001).

[82] https://doi.org/10.25405/data.ncl.20438823.v1.